



Crystal plasticity FE modeling of Ti alloys for a range of strain-rates. Part I: A unified constitutive model and flow rule

Ahmad Shahba^a, Somnath Ghosh^{b,*}

^a Civil Engineering Department, Johns Hopkins University, United States

^b Departments of Civil and Mechanical Engineering, Johns Hopkins University, United States

ARTICLE INFO

Article history:

Received 5 July 2016

Received in revised form 29 August 2016

Available online 12 September 2016

Keywords:

Unified flow rule

B. Crystal plasticity

B. Polycrystalline material

B. Constitutive behaviour

C. Finite elements

ABSTRACT

The deformation and failure response of many polycrystalline metallic materials is strongly dependent on the strain-rate. For an applied strain-rate, different points in the material microstructure can undergo strain-rates that differ by orders of magnitude depending on location and deformation history. Dislocation motion in metals is governed by the thermally-activated and drag-dominated processes under low and high rates of deformation, respectively. Commonly used flow rules, e.g the phenomenological power law or the linear viscous drag models are generally applicable to a limited range of strain-rates, without transcending these rates. To enable this transition in a seamless manner, this two part paper develops a unified constitutive model and an image-based crystal plasticity finite element model for polycrystalline *hcp* metals. The first part develops a dislocation density-based crystal plasticity constitutive relation with a unified flow rule by combining the thermally-activated and drag-dominated stages of dislocation slip, suitable for modeling deformation at a wide range of strain-rates. The model is explicitly temperature-dependent, making it appropriate for simulating high rate deformations, where temperature increases locally with plastic deformation due to the adiabatic heating. The unified model is used to study rate-sensitivity of flow stress in single crystal and polycrystalline titanium alloy, Ti-7Al. An elastic overshoot, followed by a stress relaxation is observed at high strain-rates in single crystals. For the polycrystalline simulations, the model effectively captures the increase in rate sensitivity at high strain-rates.

© 2016 Elsevier Ltd. All rights reserved.

1. Introduction

Titanium alloys are widely used in various industrial applications like compressor blades of jet engines or armor of ground combat vehicles (Montgomery et al., 1997), due to their superior properties such as high strength to weight ratio, high fracture toughness, as well as good corrosion resistance. The extensive commercial use of these alloys that have a predominantly hexagonal close-packed (*hcp*) crystalline structure, has motivated researchers to study their mechanical responses over a wide range of strain-rates and temperatures. For example, high strain-rate behavior, such as in ballistic impact problems, have been investigated by Follansbee and Gray (1989), Chichili et al. (1998), Ravichandran et al. (2002), Khan et al. (2004, 2007) and Khan and Yu (2012), while low to moderate strain-rate studies in cyclic and dwell fatigue conditions have been conducted in

* Corresponding author. 3400 N. Charles St., Baltimore, MD 21218, United States. Fax: +1 410 516 7473.

E-mail address: sgghosh20@jhu.edu (S. Ghosh).

Sinha et al. (2007) and Pilchak (2013). When modeling for different applied rates, it is important to realize that even if the loading is at a certain strain-rate (high or low), different points in the material microstructure may undergo a wide range of strain-rates depending on the material point location and deformation history. For instance, in microstructures of *hcp* Ti alloys with significant slip system resistance anisotropy, large strain gradients can develop between *soft* and *hard* grains, even with moderate applied strain-rates (Hasija et al., 2003; Deka et al., 2006; Venkataramani et al., 2007). This can lead to locally large strain-rates in their polycrystalline microstructures. Similarly, a polycrystalline microstructure that is macroscopically subjected to high strain-rates can locally undergo location-dependent lower rates of deformation, especially near stationary boundaries. Conventionally used rate-dependent plasticity models are incapable of smoothly transitioning across strain-rates. Thus, it is desirable to develop unified constitutive relations from consideration of physics-based mechanisms that can transcend a wide range of strain-rates without having to change constitutive parameters or models.

Plastic deformation in polycrystalline microstructures of Ti alloys are strongly dependent on the grain morphology and crystallographic lattice orientations. This, in part, is attributed to the large differences in the critical resolved shear stress (CRSS) for different *hcp* slip systems. For example, the CRSS of the first and second order $\langle c + a \rangle$ pyramidal systems have been shown to be $\sim 2\text{--}4$ times higher than those of the basal and prism $\langle a \rangle$ systems (Li et al., 2013; Hasija et al., 2003). This difference can cause localized stress concentrations leading to crack nucleation in creep loading and dwell fatigue (Hasija et al., 2003; Venkataramani et al., 2007, 2008; Anahid et al., 2011). Crystal plasticity finite element method (CPFEM) is conventionally used to model deformation and failure in these alloys using a variety of constitutive laws (Schoenfeld and Kad, 2002; Thomas et al., 2012; Hasija et al., 2003; Khan et al., 2004; Deka et al., 2006; Venkataramani et al., 2007; Alankar et al., 2011; Dunne et al., 2007). The predictive capability of CPFEM models is strongly dependent on the accuracy of constitutive models along with their flow rules, which express the slip-rate on crystallographic glide planes in terms of the resolved shear stress and other evolving internal state variables.

Various forms of the flow rule have been proposed in the literature. Among the most commonly used flow rules are (i) the phenomenological power law model (Peirce et al., 1982), (ii) the Arrhenius-type activation energy-based model (Kocks et al., 1975) and (iii) the linear model (Kocks et al., 1975). The power law model expresses the plastic slip-rate on a slip system α with a power law dependence on the resolved shear stress and the slip system deformation resistances (Peirce et al., 1982; Anahid et al., 2011; Cheng and Ghosh, 2015) as:

$$\dot{\gamma} = \dot{\gamma}_0^\alpha \left| \frac{\tau^\alpha - s_a^\alpha}{s_*^\alpha} \right|^{\frac{1}{m}} \text{sign}(\tau^\alpha - s_a^\alpha) \quad (1)$$

where s^α is the temperature-dependent critical shear resistance that is comprised of a thermally activated obstacle to slip s_*^α and a part due to the athermal obstacles s_a^α , τ^α is the resolved shear stress on a slip system, m is the strain-rate sensitivity exponent, and $\dot{\gamma}_0^\alpha$ is the reference slip rate. This flow rule, that implicitly accounts for temperature, is appropriate for modeling low to moderate strain-rates in the range $< 10^4 \text{ s}^{-1}$. The Arrhenius-type activation energy-based model (Kocks et al., 1975; Keshavarz and Ghosh, 2013) is of the form:

$$\dot{\gamma} = \dot{\gamma}_0^\alpha \exp \left\{ -\frac{Q_{slip}^\alpha}{k_B T} \left[1 - \left(\frac{|\tau^\alpha - s_a^\alpha|}{s_*^\alpha} \right)^p \right]^q \right\} \text{sign}(\tau^\alpha - s_a^\alpha) \quad (2)$$

where exponents p and q depend on the shape of local obstacles, Q_{slip}^α is the thermal activation energy, k_B is the Boltzmann constant and T is the temperature. The model explicitly accounts for the temperature in the thermally-activated processes governing dislocation glide, and is also applicable to deformations at low to moderate strain-rates. Its explicit dependence on the temperature makes it effective for simulating temperature-sensitive phenomena. Finally, at very high strain-rates exceeding 10^4 s^{-1} , the dislocation motion is dominated by viscous drag-dominated processes. Correspondingly, the flow rule in this range is expressed as a linear function of the effective resolved shear stress (Kocks et al., 1975) as:

$$\dot{\gamma} = \dot{\gamma}_0^\alpha \frac{|\tau^\alpha - s_a^\alpha| b^\alpha}{B(T)} \quad (3)$$

where b^α is the magnitude of the Burgers vector and $B(T)$ is the temperature dependent viscous drag coefficient.

This paper is aimed at developing a unified flow rule that can transcend the range of strain-rates corresponding to the progression from thermally-activated to drag-dominated stages of dislocation motion. Fig. 1 demonstrates the deformation mechanisms for Ti alloys, in which screw dislocations glide by a double-kink mechanism in multiple stages. The thermally-activated stage corresponds to the nucleation of the kink pair whereas the drag-dominated stage corresponds to the broadening of the kink pair and moving the dislocation line to the next Peierls valley. The flow rule to be developed will account for the time lapsed in each stage of dislocation glide and the distance dislocation; i.e. the distance between two consecutive Peierls hills in the glide plane.

There is a body of work in the literature on unified flow rules that are based on alternative formulations of average velocity of dislocations. Frost and Ashby (1971) were the first to propose a dislocation velocity formulation based on combining thermal activation and drag mechanisms. Inertial models of dislocations have been developed to model plasticity in

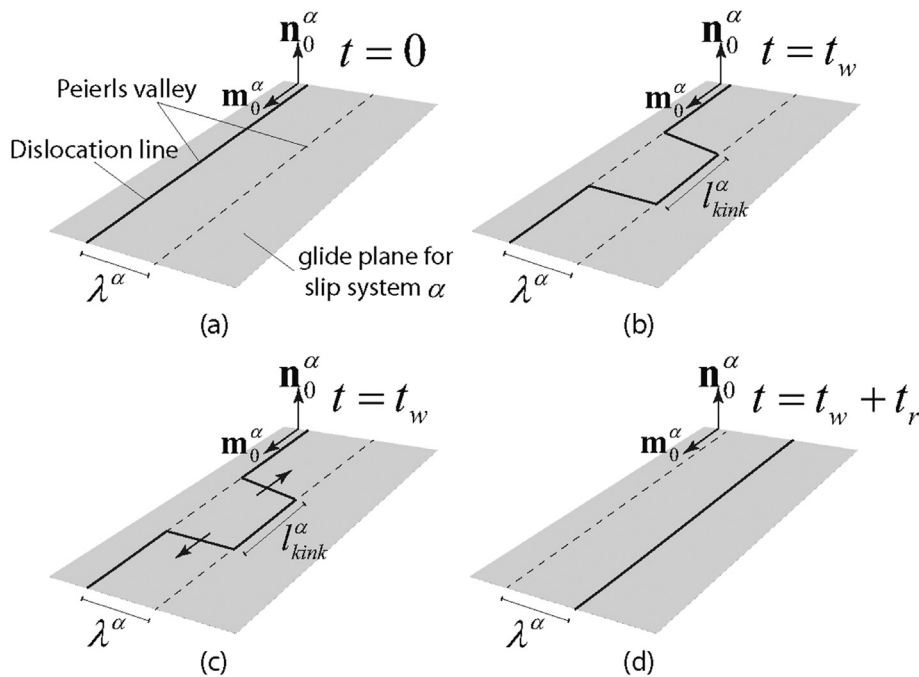


Fig. 1. Illustration of a screw dislocation motion over Peierls hills in the glide plane via a double-kink mechanism: (a) dislocation lying in a Peierls valley, (b) nucleation of kink-pair due to thermal activation, (c) kink-pairs moving apart under drag forces, and (d) dislocation moving to the next Peierls valley.

superconductors by Isaac and Granato (1988). Hiratani and Nadgorny (2001) have developed a unified model to study dislocation motion in 2D through an array of obstacles in a *fcc* metal. A similar unified model has been implemented in a discrete dislocation dynamics code to model dislocation behavior in *fcc* metals under creep conditions in Hiratani et al. (2003). Unified flow rules have been developed in the context of macroscale J_2 plasticity for modeling deformation behavior of *bcc* vanadium and tantalum (Barton et al., 2011; Becker et al., 2009). Recently (Austin and McDowell, 2011), and (Lloyd et al., 2014) have developed unified flow rules to model viscoplastic deformation in *fcc* alloys under shock loading. Most of the developments of unified flow rules have been in the realm of analytical models or discrete dislocation motion in a 2D array of obstacles. There are very few studies that have investigated the capability of these unified flow rules for crystal plasticity-based modeling of deformation in polycrystalline aggregates.

This two part paper is aimed at developing a unified crystal plasticity constitutive model and flow rule with implementation in a CPFE framework for modeling deformation in *hcp* Ti alloys subjected to a wide range of strain-rates. The first part develops the constitutive relations and discusses its CPFE implementation in Section 2. Evolution of dislocation densities and the effects of adiabatic heating on localized deformation are studied in Sections 2.1.1 and 3 respectively. Implementation in the crystal plasticity constitutive models is explained in Section 4, while Section 5 provides some numerical results demonstrating the capability of the proposed model.

2. Crystal plasticity model for a range of strain-rates

The crystal plasticity model developed in this study is for single-phase Ti alloys such as α -Ti-6Al and α -Ti-7Al with a *hcp* crystal structure. Fig. 2 shows the crystal structure with atoms stacked in an axial ratio of ~ 1.587 for titanium (Balasubramanian and Anand, 2002; Hasija et al., 2003). Plastic deformation in these alloys occurs predominantly by dislocation slip, where dislocations are distributed non-homogeneously in planar arrays due to short range ordering of Ti and Al atoms on the *hcp* lattice (Neeraj and Mills, 2001). Dislocation slip in *hcp* crystals occurs on 5 different families of slip systems as shown in Fig. 2. This corresponds to a total of 30 possible slip systems. Differential slip on these systems results in strong anisotropic behavior of Ti alloys, both in elasticity and plasticity. The $\langle a \rangle$ - basal and prism slip families have the lowest critical resolved shear stress (CRSS), making them the most active slip families. The $\langle c + a \rangle$ - pyramidal slip families have the largest CRSS, $\sim 2 - 4$ times that of the basal or prism slip systems (Li et al., 2013). The proposed constitutive model is developed for finite deformation under general non-isothermal conditions. While deformation twinning has been observed in pure Ti at temperatures below 500°C (Chichili et al., 1998; Morrow et al., 2016), the alloying of Ti with Al inhibits this process. Ti alloyed with 6% Al is found not to twin even at temperatures as low as 100 K (Paton et al., 1976; Williams et al., 2002). Hence, twinning is not considered in the constitutive model.

As illustrated in Fig. 3, the total deformation gradient \mathbf{F} is multiplicatively decomposed into elastic, thermal and plastic components (Clayton, 2005; Meissonnier et al., 2001), expressed as:

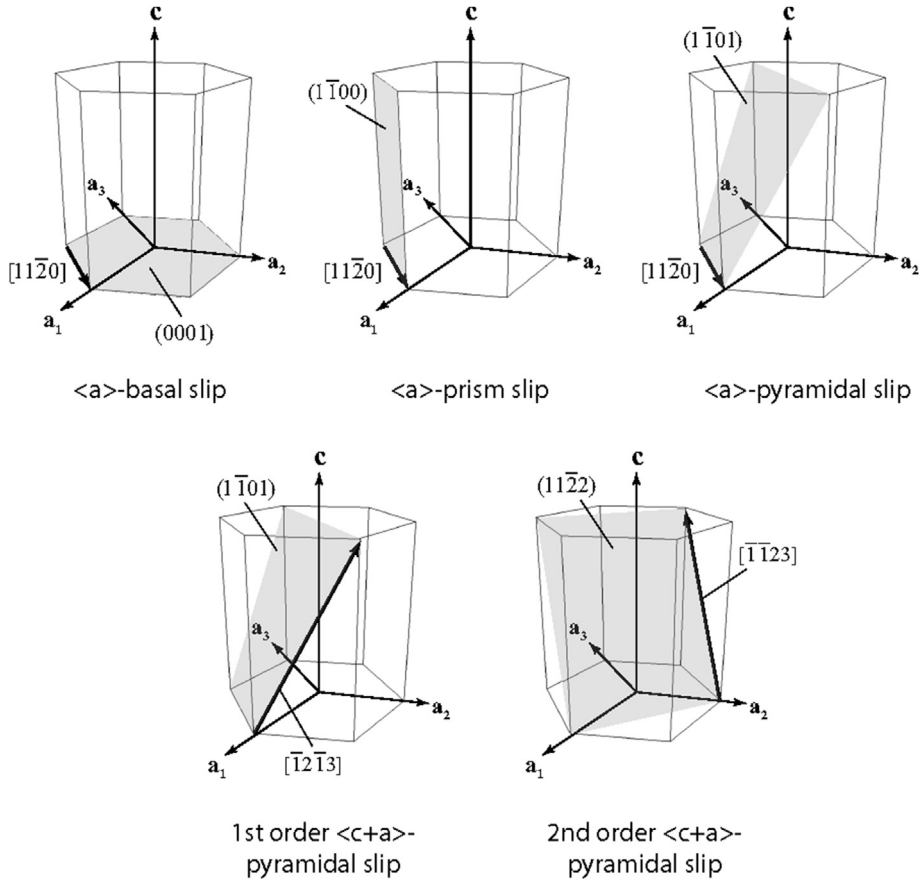


Fig. 2. Schematic view of non-orthogonal base vectors $\{a_1, a_2, a_3, c\}$ and slip system families in hcp metals and alloys.

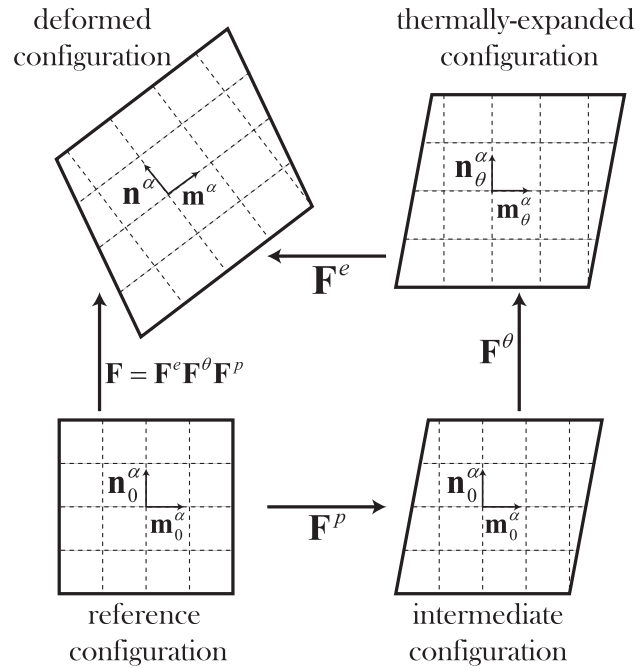


Fig. 3. Multiplicative decomposition of the total deformation gradient \mathbf{F} into elastic \mathbf{F}^e , thermal \mathbf{F}^θ and plastic \mathbf{F}^p components.

$$\mathbf{F} = \mathbf{F}^e \mathbf{F}^\theta \mathbf{F}^p \quad (4)$$

where \mathbf{F}^e accounts for the elastic stretch and rigid body rotations. \mathbf{F}^θ represents the deformation of the crystal lattice due to temperature changes that evolves as (Lee et al., 1997):

$$\dot{\mathbf{F}}^\theta = \dot{T} \boldsymbol{\alpha} \mathbf{F}^\theta \quad (5)$$

where \dot{T} is the rate of temperature change and $\boldsymbol{\alpha}$ is an anisotropic thermal expansion coefficient tensor. The latter can reduce to a diagonal matrix if expressed in the material crystallographic coordinate system. *Ab initio* calculations in Nie and Xie 2007 and Souvatzis et al. (2007) and experimental observations in Nizhankovskii et al. (1994) have corroborated the existence of anisotropic thermal expansion coefficient tensor for α Ti alloys over a wide range of temperatures. The component \mathbf{F}^p corresponds to the isochoric plastic deformation due to dislocation slip, with $\det \mathbf{F}^p = 1$. The \mathbf{F}^p mapping neither distorts nor rotates the crystal lattice. Using the kinematics of dislocation glide, the plastic velocity gradient tensor \mathbf{L}^p in the intermediate configuration is obtained as (Asaro and Rice, 1977):

$$\mathbf{L}^p = \dot{\mathbf{F}}^p \mathbf{F}^{p-1} = \sum_{\alpha=1}^{n_{\text{slip}}} \dot{\gamma}^\alpha \mathbf{m}_0^\alpha \otimes \mathbf{n}_0^\alpha \quad (6)$$

where $\dot{\gamma}^\alpha$ is the slip rate, and \mathbf{m}_0^α and \mathbf{n}_0^α are respectively the slip direction and slip plane normal in the reference configuration for the slip system α . The summation is over all the slip systems $n_{\text{slip}} = 30$ for *hcp* crystals. The stress-strain law in the thermally-expanded configuration is given as:

$$\mathbf{S} = \det(\mathbf{F}^e) \mathbf{F}^{e-1} \boldsymbol{\sigma} \mathbf{F}^{e-T} = \mathbb{C} : \mathbf{E}^e \quad (7)$$

where \mathbb{C} is the fourth order anisotropic elasticity tensor, \mathbf{S} denotes the second Piola-Kirchhoff stress in the thermally-expanded configuration, $\mathbf{E}^e = \frac{1}{2}(\mathbf{F}^{eT} \mathbf{F}^e - \mathbf{I})$ is its work-conjugate elastic Green–Lagrange strain, and $\boldsymbol{\sigma}$ is the Cauchy stress. It is noteworthy that equation (7) must be augmented with higher-order pressure-dependent elasticity tensors to model shock problems involving high pressures as shown in Lloyd et al. (2014).

2.1. The proposed unified flow rule

The flow rule in a crystal plasticity constitutive model expresses slip-rates as a function of the local stress state and relevant internal state variables. Dislocation motion on glide planes is generally controlled by both thermal activation and drag mechanisms. The relative strength of these mechanisms changes with the level of stresses and strain-rate. Thermally-activated processes are the dominant mechanism up to strain rates of 10^4 s^{-1} while drag processes control the dislocation glide at strain rates above 10^4 s^{-1} . The physics-based unified flow rule derived here, represents a combination of thermally-activated and drag dominated mechanisms, while reducing to the activation energy-based and linear flow rules as limiting cases.

The Orowan equation expresses the slip-rate on slip system α in terms of dislocation density ρ^α and the average dislocation velocity v^α as:

$$\dot{\gamma}^\alpha = \rho^\alpha b^\alpha v^\alpha \text{sign}(\tau^\alpha) \quad (8)$$

where b^α is the magnitude of Burgers vector and τ^α is the slip system resolved shear stress calculated as:

$$\tau^\alpha = \det(\mathbf{F}^\theta) \mathbb{C}^e \mathbf{S} : (\mathbf{F}^\theta \mathbf{m}_0^\alpha \otimes \mathbf{n}_0^\alpha \mathbf{F}^{\theta-1}) \quad (9)$$

$\mathbb{C}^e = \mathbf{F}^{eT} \mathbb{C} \mathbf{F}^e$ is the right elastic Cauchy-Green deformation tensor.

Experimental observations in Williams et al. (2002) and Brandes (2008) have concluded that predominantly screw dislocations are responsible for plastic deformation in Ti alloys. These screw dislocations move over the Peierls hills in the glide plane by the double-kink mechanism that involves thermally-activated nucleation of kink pairs. Assuming nucleation of one kink pair per dislocation line, the dislocation motion by this mechanism takes place in two stages as shown in Fig. 1. In the first stage, the dislocation lies in a Peierls valley and waits for a period *waiting time* t_w^α until a successful local thermal activation takes place and a pair of kinks with a separation distance of l_{kink}^α nucleates and moves to the next Peierls valley (Guyot and Dorn, 1967). In the subsequent drag-dominated stage, the kinks move apart and bring the whole dislocation line to the next Peierls valley (Kocks et al., 1975). The time spent in this stage is *running time* t_r^α . The average dislocation velocity can then be formulated in terms of the waiting and running times as (Hiratani et al., 2003):

$$v^\alpha = \frac{\lambda^\alpha}{t_w^\alpha + t_r^\alpha} \quad (10)$$

where λ^α is the spacing between two consecutive Peierls valleys that may be approximated as b^α .

Since t_w^α corresponds to the thermally-activated nucleation of a kink pair, it is defined by a temperature-dependent Arrhenius-type relationship as (Tang et al., 1998):

$$t_w^\alpha = \left[2 \frac{\nu_D b^\alpha}{l_{kink}^\alpha} \frac{l^\alpha}{l_{kink}^\alpha} \exp\left(-\frac{Q_{slip}^\alpha}{K_B T}\right) \sinh\left(\frac{|\tau^\alpha| - \tau_{ath}^\alpha}{\tau_{th}^\alpha}\right) \right]^{-1} \quad (11)$$

in which l^α is the average length of a straight dislocation line that is inversely proportional to the square root of the forest dislocation population ρ_F^α . This is expressed as $l^\alpha = c_l^\alpha / \sqrt{\rho_F^\alpha}$, where c_l^α is a material constant (Alankar et al., 2011). K_B is the Boltzmann constant and ν_D is the Debye frequency, which is known to be $9.13 \times 10^{13} \text{ s}^{-1}$ for titanium. Q_{slip}^α is the effective activation energy for dislocation slip. Experimental observations in Akhtar and Teghtsoonian (1975) and Tanaka and Conrad (1972) suggest that the effective activation energy is generally temperature-dependent. Correspondingly a temperature dependent form:

$$Q_{slip}^\alpha(T) = Q_{ref}^\alpha + c_Q^\alpha \left(T/T_{ref} - 1 \right)^{p_Q^\alpha} \quad (12)$$

is adopted in this paper, where c_Q^α and p_Q^α are material constants and Q_{ref}^α and T_{ref} are respectively the reference effective activation energy and temperature. The term $\frac{\nu_D b^\alpha}{l_{kink}^\alpha}$ corresponds to the attempt frequency for nucleation of a kink pair and the term $\frac{l^\alpha}{l_{kink}^\alpha}$ is the number of competing sites for kink nucleation on the dislocation line. τ_{ath}^α and τ_{th}^α are respectively the athermal and thermal resistances to dislocation motion on slip system α , detailed in Section 2.1.2.

The running time t_r^α corresponds to the stage, where retarding drag forces due to the phonon-dislocation interactions govern dislocation motion, effectively broadening the kink band. It is written in terms of viscous drag velocity v_d^α as (Hiratani et al., 2003; Hiratani and Nadgorny, 2001):

$$t_r^\alpha = \frac{\lambda^\alpha}{v_d^\alpha} \quad (13)$$

Depending on the temperature, various types of phonon-dislocation interactions, e.g. flutter, scattering, or radiation mechanisms, are possible (Kocks et al., 1975; Hiratani and Nadgorny, 2001). These interactions yield a temperature-dependent drag coefficient B_0 , given by the relation (Kocks et al., 1975):

$$B_0 = \frac{c_d K_B T}{\nu_s b^{\alpha 2}} \quad (14)$$

where ν_s is the shear wave speed and c_d is the drag constant. Assuming that the change in rate-sensitivity of the flow stress occurs around 10^5 s^{-1} , as observed in experiments on titanium alloys (Casem, 2015), the drag coefficient is derived to be $c_d = 45$. Given the ratio of the effective dislocation line mass density to the drag coefficient B_0 that represents a decaying time scale is very small, the equation of motion for a unit length of dislocation line is solved to yield the viscous drag velocity as (Hansen et al., 2013):

$$v_d^\alpha = \frac{(|\tau^\alpha| - \tau_{ath}^\alpha) b^\alpha}{B_0} \quad (15)$$

In Austin and McDowell (2011), the drag coefficient has been modified to ensure that the dislocation drag velocity does not exceed the shear wave speed, by incorporating relativistic effects as:

$$B = \frac{B_0}{1 - \left(\frac{v_d^\alpha}{\nu_s} \right)^2} \quad (16)$$

This modification implies that as the dislocation drag velocity v_d^α approaches the shear wave speed, the drag coefficient B grows to be large. Consequently very large resolved shear stresses are needed for dislocation glide. Replacing B_0 in equation (15) with B and solving for v_d^α , the modified dislocation drag velocity is obtained as (Austin and McDowell, 2011):

$$v_d^\alpha = \nu_s \left[\sqrt{1 + \left(\frac{B_0 \nu_s}{2(|\tau^\alpha| - \tau_{ath}^\alpha) b^\alpha} \right)^2} - \frac{B_0 \nu_s}{2(|\tau^\alpha| - \tau_{ath}^\alpha) b^\alpha} \right] \quad (17)$$

Substituting equations (13) and (11) into equation (10), the expression for the unified average dislocation velocity, incorporating both thermally-activated and drag-dominated processes, is written as:

$$v^\alpha = \frac{v_d^\alpha}{\frac{v_d^\alpha}{\lambda} \left[2 \frac{v_D^\alpha b^\alpha}{l_{\text{kink}}^\alpha} \frac{l^\alpha}{l_{\text{kink}}^\alpha} \exp\left(-\frac{Q_{\text{slip}}^\alpha}{K_B T}\right) \sinh\left(\frac{|\tau^\alpha| - \tau_{\text{ath}}^\alpha}{\tau_{\text{th}}^\alpha}\right) \right]^{-1} + 1} \quad (18)$$

Remark 1. For low strain-rate deformations corresponding to lower stress levels, $t_r^\alpha \ll t_w^\alpha$, i.e. $t_r^\alpha \approx 0$. In this case, the average dislocation velocity in equation (10) reduces to:

$$v^\alpha = \frac{\lambda^\alpha}{t_w^\alpha} = 2\lambda^\alpha \frac{v_D^\alpha b^\alpha}{l_{\text{kink}}^\alpha} \frac{l^\alpha}{l_{\text{kink}}^\alpha} \exp\left(-\frac{Q_{\text{slip}}^\alpha}{K_B T}\right) \sinh\left(\frac{|\tau^\alpha| - \tau_{\text{ath}}^\alpha}{\tau_{\text{th}}^\alpha}\right) \quad (19)$$

As is expected, this dislocation velocity expression is used in the Arrhenius type thermal activation-based flow rule.

Remark 2. At high strain-rates corresponding to high stress levels, $t_w^\alpha \ll t_r^\alpha$, i.e. $t_w^\alpha \approx 0$. Correspondingly for these drag-dominated processes the average dislocation velocity in equation (10) reduces to:

$$v^\alpha = \frac{\lambda^\alpha}{t_r^\alpha} = v_d^\alpha = \frac{(|\tau^\alpha| - \tau_{\text{ath}}^\alpha) b^\alpha}{B_0} \quad (20)$$

which is the velocity used in the linear flow rule.

The slip rates on different slip systems can then be derived using equation (8) with known dislocation densities, whose evolution will be discussed in Section 2.1.1.

The average dislocation velocity for the unified flow rule in equation (18), as well as the velocities for the thermally-activated and drag-dominated dislocation motions in equations (19) and (20) respectively are plotted in Fig. 4(a,b). In Fig. 4(b), the velocities are plotted on a log-scale for improved clarity. The resolved shear stress is increased to calculate the average dislocation velocity as a function of stress at room temperature $T = 300$ K. The forest dislocation density is kept fixed at $30.49 \mu\text{m}^{-2}$. The parameters used to simulate these plots are given in Table 1. The material constants used are $c_{\text{ath}}^\alpha = 0.8$, $c_{\text{act}}^\alpha = 0.7$ and $c_l^\alpha = 8.0$. At lower stresses and strain-rates, the velocity profile by the unified rule agrees well with the velocity predicted by the activation energy based rule. With increasing stresses and strain-rates, the rate of successful thermal activation is boosted and t_w^α decreases exponentially. Consequently at around 90 m/s, the velocity by the unified rule smoothly transitions to the velocity by the linear rule for the drag-dominated dislocation motion. This transition point is close to predictions of ~ 100 m/s made by a multi-scale strength model for screw dislocations in tantalum (Barton et al., 2011).

2.1.1. Evolution of dislocation densities

The dislocation density-based crystal plasticity framework accounts for material hardening in terms of the interaction and entanglement of dislocations on different slip systems. Dislocation populations are traditionally divided into two classes, viz. statistically stored dislocations (SSDs) that are characterized by a net vanishing Burgers vector, and geometrically necessary

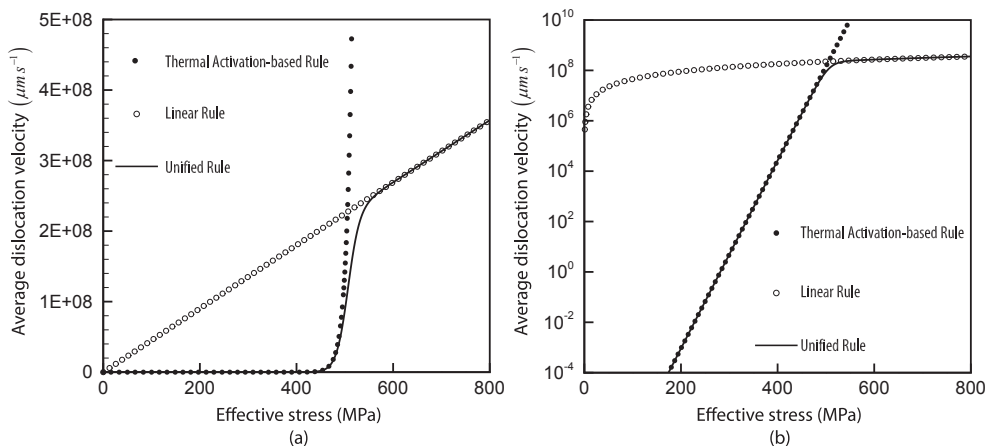


Fig. 4. Comparison of the average dislocation velocity by the unified flow rule with the velocities with the thermally-activated and drag-dominated dislocation motions, plotted on (a) regular scale and (b) log-scale.

Table 1

Parameters for basal slip system at room temperature.

Parameters (unit)	Q_{ref}^α (J)	b^α (m)	l_{kink}^α (b^α)	ν_D (s^{-1})	ν_s (ms^{-1})
Value	2.1×10^{-19}	2.94×10^{-10}	20	9.13×10^{13}	3312

dislocations (GNDs) characterized by a non-zero net Burgers vector (Arsenlis and Parks, 1998). With deformation, SSDs evolve by various mechanisms such as multiplication, thermal and athermal annihilation, etc. (Ma et al., 2006). GNDs on the other hand, correspond to the storage of polarized dislocation densities and account for crystal lattice curvatures near grain boundaries of polycrystalline aggregates.

The evolution of SSDs is predominantly governed by two competing mechanisms of dislocation multiplication and annihilation. Other less dominant mechanisms are ignored in the present formulation. The multiplication rate on a slip system α has been related to the inverse of dislocation length (or equivalently square root of dislocation density) in Essmann and Mughrabi (1979) as:

$$\dot{\rho}_{mult}^\alpha = c_{multi}^\alpha \sqrt{\rho^\alpha} |\dot{\gamma}^\alpha| \quad (21)$$

where c_{multi}^α is a material constant. This equation was originally derived for *fcc* metals with the assumption of emission of rectangular shaped dislocation loops from dislocation sources. This work makes the same assumption for the *hcp* alloys. Dislocations of opposite sign can annihilate each other athermally if they come within a critical distance. The rate of athermal annihilation is given as (Essmann and Mughrabi, 1979; Alankar et al., 2011):

$$\dot{\rho}_{anni}^\alpha = c_{annih}^\alpha \rho^\alpha |\dot{\gamma}^\alpha| \quad (22)$$

with c_{annih}^α as a material constant. The rate of dislocation evolution is written as:

$$\dot{\rho}^\alpha = \dot{\rho}_{mult}^\alpha - \dot{\rho}_{anni}^\alpha \quad (23)$$

following the simplified form in Mecking and Kocks (1981).

GNDs are attributed to plastic strain incompatibility across grain boundaries. For *hcp* crystals, plastic anisotropy in slip systems result in strong crystallographic orientation-dependent plastic response. Large plastic strain gradients at grain boundaries with high crystallographic misorientation lead to the accumulation of GNDs at these locations. The Nye dislocation tensor Λ is a measure of plastic incompatibility in the intermediate configuration and is expressed as:

$$\Lambda = -(\nabla_X \times \mathbf{F}^{pT})^T \quad (24)$$

where ∇_X is the gradient operator in the reference coordinate system. The Nye dislocation tensor is equivalently expressed in terms of GNDs as (Dai, 1997):

$$\Lambda = \sum_{\alpha=1}^{n_{slip}} b^\alpha (\rho_{GNDs}^\alpha \mathbf{m}_0^\alpha \otimes \mathbf{m}_0^\alpha + \rho_{GNDet}^\alpha \mathbf{m}_0^\alpha \otimes \mathbf{t}_0^\alpha + \rho_{GNDen}^\alpha \mathbf{m}_0^\alpha \otimes \mathbf{n}_0^\alpha) \quad (25)$$

where ρ_{GNDs}^α , ρ_{GNDen}^α and ρ_{GNDet}^α are vector components of the GND density on slip system α with Burgers vector along \mathbf{m}_0^α , and line tangents respectively along directions \mathbf{m}_0^α , \mathbf{n}_0^α and $\mathbf{t}_0^\alpha = \mathbf{m}_0^\alpha \times \mathbf{n}_0^\alpha$ (Ma et al., 2006). In general, there are $3 \times n_{slip}$ or 90 unknown GND densities for *hcp* crystals. However, there are only 9 independent ρ_{GNDs}^α , 24 independent ρ_{GNDet}^α and 30 independent ρ_{GNDen}^α , corresponding to a total of 63 unknown GND density components. From equations (24) and (25), yields:

$$\hat{\Lambda} = \mathbf{A} \rho_{GND} \quad (26)$$

in which $\hat{\Lambda}$ is the 9×1 vector form of Λ , \mathbf{A} is a 9×36 matrix containing the basis vectors $\mathbf{m}_0^\alpha \otimes \mathbf{m}_0^\alpha$, $\mathbf{m}_0^\alpha \otimes \mathbf{t}_0^\alpha$ and $\mathbf{m}_0^\alpha \otimes \mathbf{n}_0^\alpha$ and ρ_{GND} is a 63×1 column vector of unknown independent GND components. It is clear that equation (26) is an under-determined system of linear equations that does not have a unique solution. To regularize this, a functional is set up from geometric considerations given in Arsenlis and Parks (1998) and Cheng and Ghosh (2015) as:

$$\mathcal{F}(\rho_{GND}, \lambda) = \rho_{GND}^T \rho_{GND} + \lambda^T (\mathbf{A} \rho_{GND} - \hat{\Lambda}) \quad (27)$$

Here λ is the vector of Lagrange multipliers. Minimizing the functional \mathcal{F} , the GND densities are obtained as

$$\rho_{GND} = \mathbf{A}^T (\mathbf{A} \mathbf{A}^T)^{-1} \hat{\Lambda} \quad (28)$$

GNDs in the CP framework render the model size-dependent and non-local, since the Nye dislocation tensor is derived in terms of the gradient of \mathbf{F}^p field in equation (24).

2.1.2. Slip system resistances

The SSD and GND densities are internal state variables in the unified flow rule that contribute to the slip system hardening. The athermal and thermal resistances to dislocation motion on slip system α are given as (Ma et al., 2006):

$$\tau_{ath}^\alpha = c_{ath}^\alpha \mu^\alpha b^\alpha \sqrt{\rho_p^\alpha} + s_0^\alpha \quad (29a)$$

$$\tau_{th}^\alpha = \frac{K_B T}{c_{act}^\alpha l_{kink}^\alpha b^{\alpha 2}} \quad (29b)$$

where c_{ath}^α and c_{act}^α are model parameters and μ^α is the projection of the shear modulus G on the slip system α . The denominator $c_{act}^\alpha l_{kink}^\alpha b^{\alpha 2}$ in equation (29b) corresponds to the activation volume and s_0^α is the grain size-dependent initial resistance, which contributes to the athermal resistance (Nemat-Nasser et al., 1999). It follows a Hall-Petch type relationship established in Venkataramani et al. (2007) as:

$$s_0^\alpha = s_{0*}^\alpha + \frac{K^\alpha}{\sqrt{D_g}} \quad (30)$$

where s_{0*}^α and D_g are the initial slip system resistance and equivalent grain diameter respectively. $K^\alpha = \sqrt{\frac{(2-\nu)\pi\tau^*Gb^\alpha}{2(1-\nu)}}$ is a Hall–Petch coefficient with ν , G and τ^* as the Poisson's ratio, shear modulus and grain boundary barrier strength respectively. For Ti alloys, the value $\tau^* = 0.01G$ has been given in Venkataramani et al. (2007). In equation (29a) ρ_p^α is the parallel dislocation density on the slip system α , while ρ_F^α corresponds to the forest dislocation density perpendicular to it. The parallel and forest dislocation densities are calculated as (Keshavarz and Ghosh, 2013):

$$\rho_p^\alpha = \sum_{\beta=1}^{n_{slip}} \chi^{\alpha\beta} \left[\left| \rho_{GNDs}^\beta \sin(\mathbf{n}_0^\alpha, \mathbf{m}_0^\beta) \right| + \left| \rho_{GNDet}^\beta \sin(\mathbf{n}_0^\alpha, \mathbf{t}_0^\beta) \right| + \left| \rho_{GNDen}^\beta \sin(\mathbf{n}_0^\alpha, \mathbf{n}_0^\beta) \right| + \left| \rho^\beta \sin(\mathbf{n}_0^\alpha, \mathbf{m}_0^\beta) \right| \right] \quad (31a)$$

$$\rho_F^\alpha = \sum_{\beta=1}^{n_{slip}} \chi^{\alpha\beta} \left[\left| \rho_{GNDs}^\beta \cos(\mathbf{n}_0^\alpha, \mathbf{m}_0^\beta) \right| + \left| \rho_{GNDet}^\beta \cos(\mathbf{n}_0^\alpha, \mathbf{t}_0^\beta) \right| + \left| \rho_{GNDen}^\beta \cos(\mathbf{n}_0^\alpha, \mathbf{n}_0^\beta) \right| + \left| \rho^\beta \cos(\mathbf{n}_0^\alpha, \mathbf{m}_0^\beta) \right| \right] \quad (31b)$$

where $\chi^{\alpha\beta}$ is an interaction factor, defining the strengthening effect of slip system β on slip system α . $\chi^{\alpha\beta}$ is taken as 1 in this work. In the last term on the RHS of equations (31a) and (31b), the angle between \mathbf{n}_0^α and \mathbf{m}_0^β is used to project ρ^β onto the slip system α . \mathbf{m}_0^β is used here since the tangent line is parallel to the Burgers vector for screw dislocations.

2.2. A phenomenological flow rule for comparison

Rate-dependent phenomenological flow rules, especially those using the power law, have been used to describe crystallographic slip-rates for metals and alloys in various studies e.g. in Asaro and Rice (1977), Balasubramanian and Anand (2002), Hasija et al. (2003) and Deka et al. (2006). In these rules, the average velocity of dislocations has a power-law dependence on the resolved shear stress, and the slip-rate is expressed as:

$$\dot{\gamma}^\alpha = \dot{\gamma}_0^\alpha \left(\frac{|\tau^\alpha| - \tau_{ath}^\alpha}{s^\alpha} \right)^{\frac{1}{m}} \text{sign}(\tau^\alpha) \quad (32)$$

where m , $\dot{\gamma}_0^\alpha$ and s^α are respectively the rate sensitivity parameter, the reference plastic shearing rate and the resistance to dislocation glide due to the interaction with other dislocations through self and latent hardening mechanisms. For Ti alloys, the effect of SSDs on the slip system resistances are taken into account through phenomenological relationships (Venkataramani et al., 2007; Cheng and Ghosh, 2015)

$$\tau_{ath}^\alpha = c_1^\alpha \mu^\alpha b^\alpha \sqrt{\rho_{GND,p}^\alpha} \quad (33a)$$

$$s^\alpha = s_0^\alpha + \int_{t'=0}^{t'=t} \sum_{\beta=1}^{n_{slip}} h^{\alpha\beta} |\dot{\gamma}^\beta| dt' + \frac{Q^\alpha}{c_2^\alpha c_3^\alpha b^{\alpha 2}} \sqrt{\rho_{GND,F}^\alpha} \quad (33b)$$

where $\rho_{\text{GND,P}}^\alpha$ and $\rho_{\text{GND,F}}^\alpha$ are respectively the parallel and forest GND densities. Material constant c_1^α is for the long-range impeding stresses arising due to GNDs, while c_2^α and c_3^α respectively correspond to the jump and obstacle width (Ma et al., 2006). For hcp crystals, these have been calibrated to be $c_1^\alpha = 0.1$, $c_2^\alpha = 0.2$ and $c_3^\alpha = 1.0$ in Cheng and Ghosh (2015). Q^α is the activation energy to overcome forest GND dislocation population, which is approximated as $Q^\alpha = 10\mu^\alpha b^\alpha$ for hcp crystals in Cheng and Ghosh (2015). $h^{\alpha\beta}$ is the hardening matrix that accounts for self and latent hardening and is given as:

$$h^{\alpha\beta} = \chi^{\alpha\beta} h_{\text{ref}}^\beta \left| 1 - \frac{s^\beta}{s_{\text{sat}}^\beta} \right|^r \text{sign} \left(1 - \frac{s^\beta}{s_{\text{sat}}^\beta} \right) \quad \text{where } s_{\text{sat}}^\beta = \bar{s}^\beta \left| \frac{\dot{\gamma}^\beta}{\dot{\gamma}_0^\beta} \right|^n \quad (34)$$

where r , n and h_{ref}^β are material constants and \bar{s}^β denotes the saturation stress on slip system β . The phenomenological flow rule is used for comparing numerical results with the unified flow rule.

3. Adiabatic heating

Plastic deformation is an exothermic process that releases energy in the form of heat. A large fraction ($\approx 90\%$) of the energy dissipated due to the plasticity is converted into heat, while some is stored in the microstructure as stored and defect energy (Clayton, 2005; Ravichandran et al., 2002). At lower strain-rates, the localized heat generated has time to conduct away into the material. However, at high rates of deformation, the time afforded for transient heat conduction is very short. This leads to a localized increase in the temperature adiabatically. Even deformations at moderate strain-rates can lead to adiabatic heating processes (Ravichandran et al., 2002).

Temperature increase due to adiabatic heating, in turn, promotes additional plastic deformation through an increase in the rate of thermal activation. This cycle is more relevant for high strain-rate problems. The rate of temperature increase due to adiabatic heating is expressed as:

$$\dot{T} = \frac{\beta_t}{\rho \hat{c}} \dot{W}_p \quad (35)$$

where ρ is the material mass density, \hat{c} is the temperature-dependent specific heat capacity at constant volume. For Ti alloys the values are $\rho = 4428 \text{ kg/m}^3$ and $\hat{c} = 559.77 - 0.1473T + 0.00042949T^2 \text{ J/Kg}^\circ\text{K}^{-1}$ for the temperature range $278\text{K} < T < 1144\text{K}$ from Military Handbook (1998). $\dot{W}_p = \boldsymbol{\sigma} : \mathbf{d}^p$ is the plastic power per unit deformed volume, where \mathbf{d}^p is the symmetric part of the plastic velocity gradient in the current configuration $\mathbf{l}^p = \mathbf{F}^e \mathbf{F}^{\theta} \dot{\mathbf{F}}^p \mathbf{F}^{p-1} \mathbf{F}^{\theta-1} \mathbf{F}^{e-1}$. The parameter β_t corresponds to the fraction of plastic work that is converted to heat and is taken to be 0.9 in this study. While the heat energy has been largely assumed to be 90% of the plastic dissipation in studies on various metals, experimental studies e.g. in Ravichandran et al. (2002) have shown some variations. When modeling shock events (Clayton, 2010), the incorporation of thermo-elastic effects in equation (35) may be necessary, in addition to plastic work.

4. Aspects of numerical implementation and time integration algorithm

The rate-dependent crystal plasticity equations with the unified and phenomenological flow rules, discussed in section 2, are implemented in a large deformation crystal plasticity FE (CPFE) code. A few of the pertinent implementation issues are discussed here.

4.1. Stabilized, locking-free tetrahedral elements

Image-based CPFE modeling involves generation of virtual polycrystalline microstructures from experimental data, followed by discretization into finite element meshes. Discretization, conforming to the complex grain geometries, is best accomplished using 3D four-noded tetrahedral or TET4 elements. However, several FE studies on plastic deformation, e.g. in Matous and Maniatty (2004), de Souza Neto et al. (2005) and Cheng et al. (2016) have suggested that TET4 elements suffer from severe volumetric locking due to the presence of isochoric plastic deformation. Volumetric locking-induced instability is manifested in the form of over-predicted stress levels, checker-board patterned pressure fields and under-predicted displacement fields. The accuracy of CPFEM simulations is often adversely affected by this instability of TET4 elements. To alleviate this, a stabilized, volumetric locking-free element has been recently proposed in Cheng et al. (2016) for CPFEM calculations, termed as the $\bar{\mathbf{F}}$ -patch element. It is based on modifying the deformation gradient in constitutive calculations such that incompressibility is enforced over a patch of elements, rather than on an individual element. To apply this method for CPFE simulations, the entire mesh is divided into non-overlapping patches of elements. The modified deformation gradient $\bar{\mathbf{F}}_K$ for an element belonging to a patch (set of elements) \mathcal{P} i.e. $K \in \mathcal{P}$, at time $t + \Delta t$ in an incremental solution process between times t and $t + \Delta t$ is calculated as:

$$\bar{\mathbf{F}}_K(t + \Delta t) = \left[\frac{\Omega_{\mathcal{P}}^{t+\Delta t}}{\Omega_{\mathcal{P}}^0 \det \mathbf{F}_K(t + \Delta t)} \right]^{\frac{1}{3}} \mathbf{F}_K(t + \Delta t) \quad (36)$$

where $\Omega_{\mathcal{P}}^{t+\Delta t}$ and $\Omega_{\mathcal{P}}^0$ are respectively the volume of the patch in the current and undeformed configurations. The modified deformation gradient $\bar{\mathbf{F}}_K(t + \Delta t)$ is then passed on to the material subroutine for CP constitutive calculations.

4.2. Plastic strain gradient calculation

Constitutive updates are performed at the integration points of the TET4 elements. All the internal state variables and kinematic quantities such as \mathbf{F}^p are known only at these integration points. Calculation of gradients of these discretely computed internal variables are required in the constitutive updates and require special processes of evaluation. For the calculation of GNDs, the gradient of the \mathbf{F}^p field in an element requires its interpolation using element shape functions N_β as:

$$\mathbf{F}^p(\mathbf{X}) = \sum_{\beta=1}^{n_{node}} N_\beta(\mathbf{X}) \mathbf{F}_\beta^p, \quad \Rightarrow \quad \mathbf{grad} \mathbf{F}^p(\mathbf{X}) = \sum_{\beta=1}^{n_{node}} \mathbf{grad} N_\beta(\mathbf{X}) \mathbf{F}_\beta^p$$

where n_{node} is the number of nodes per element and \mathbf{F}_β^p are the nodal values. In this work, the nodal values are determined from the known values of \mathbf{F}^p at integration points by a super-convergent patch recovery **SPR** method (Zienkiewicz and Zhu, 1992). A detailed discussion on the derivation of nodal values of \mathbf{F}^p using the **SPR** technique is given in Cheng and Ghosh (2015).

4.3. Time integration of the constitutive relations

The time integration algorithm calculates internal state variable in an increment at time $t + \Delta t$ from their known values at time t , as well as the deformation gradient $\mathbf{F}(t + \Delta t) = \bar{\mathbf{F}}(t + \Delta t)$. Several time integration algorithms have been proposed in the literature for updating CP constitutive models and an excellent summary is provided in Ling et al. (2005). This work provides a semi-implicit algorithm for solving a set of six nonlinear algebraic equations, corresponding to each component of the second Piola-Kirchhoff stress. The algorithm starts with the following known or prescribed quantities in a time step from t to $t + \Delta t$.

- Kinematic quantities, viz. $\mathbf{F}(t)$, $\mathbf{F}^\theta(t)$, $\mathbf{F}^p(t)$
- Internal state variables (ISV), viz. $T(t)$, $\dot{W}_p(t)$, $s^\alpha(t)$ (only for the phenomenological flow rule) and $\rho^\alpha(t)$ (only for the unified flow rule)
- $\mathbf{F}(t + \Delta t)$

For the constitutive updates in the time interval $[t, t + \Delta t]$, the GND densities are calculated using $\mathbf{F}^p(t)$. Furthermore, it is necessary to update the temperature and thermal deformation gradient. For adiabatic process simulations, the rate of thermal deformation gradient can be obtained by substituting equation (5) in (35) to yield:

$$\dot{\mathbf{F}}^\theta = \frac{\beta_t}{\rho \hat{c}} \dot{W}_p \alpha \mathbf{F}^\theta \quad (37)$$

Integrating equation (35) over the time interval $[t, t + \Delta t]$, the temperature at time $t + \Delta t$ is found explicitly as:

$$T(t + \Delta t) = T(t) + \frac{\beta_t \dot{W}_p(t) \Delta t}{\rho \hat{c}} \quad (38)$$

and the thermal deformation gradient at $t + \Delta t$ is:

$$\mathbf{F}^\theta(t + \Delta t) = \exp \left(\alpha \frac{\beta_t \dot{W}_p(t) \Delta t}{\rho \hat{c}} \right) \mathbf{F}^\theta(t) \quad (39)$$

Similarly, \mathbf{F}^p at time $t + \Delta t$ is obtained by integrating equation (6) as:

$$\mathbf{F}^p(t + \Delta t) \approx \left(\mathbf{I} + \sum_{\alpha=1}^{n_{slip}} \Delta \gamma^\alpha \mathbf{m}_0^\alpha \otimes \mathbf{n}_0^\alpha \right) \mathbf{F}^p(t) \quad (40)$$

where $\Delta \gamma^\alpha = \dot{\gamma}^\alpha \Delta t$. Using equations (4) and (40), the elastic deformation gradient is derived as:

$$\mathbf{F}^e(t + \Delta t) = \mathbf{F}(t + \Delta t) \mathbf{F}^{p-1}(t) \left(\mathbf{I} - \sum_{\alpha=1}^{n_{slip}} \Delta \gamma^\alpha \mathbf{m}_0^\alpha \otimes \mathbf{n}_0^\alpha \right) \mathbf{F}^{\theta-1}(t + \Delta t) \quad (41)$$

Substituting $\mathbf{F}^e(t + \Delta t)$ into equation (7), a set of nonlinear equations is set up in terms of the second Piola–Kirchhoff stress as:

$$\mathbf{S}(t + \Delta t) = \mathbf{S}^{tr} - \sum_{\alpha=1}^{n_{slip}} \Delta \gamma^\alpha (\mathbf{S}(t + \Delta t), \text{ISV}) \mathbf{B}^\alpha \quad (42)$$

where

$$\tilde{\mathbf{A}} = \mathbf{F}^{p-T}(t) \mathbf{F}^T(t + \Delta t) \mathbf{F}(t + \Delta t) \mathbf{F}^{p-1}(t) \quad (43a)$$

$$\mathbf{S}^{tr} = \mathbb{C} : \left[\frac{1}{2} \left(\mathbf{F}^{\theta-T}(t + \Delta t) \tilde{\mathbf{A}} \mathbf{F}^{\theta-1}(t + \Delta t) - \mathbf{I} \right) \right] \quad (43b)$$

$$\begin{aligned} \mathbf{B}^\alpha &= \frac{1}{2} \mathbb{C} : \left[\mathbf{F}^{\theta-T}(t + \Delta t) \left(\tilde{\mathbf{A}} (\mathbf{m}_0^\alpha \otimes \mathbf{n}_0^\alpha) + (\mathbf{n}_0^\alpha \otimes \mathbf{m}_0^\alpha) \tilde{\mathbf{A}} \right) \mathbf{F}^{\theta-1}(t + \Delta t) \right] \\ &= \mathbb{C} : \left[\mathbf{F}^{\theta-T}(t + \Delta t) \tilde{\mathbf{A}} (\mathbf{m}_0^\alpha \otimes \mathbf{n}_0^\alpha) \mathbf{F}^{\theta-1}(t + \Delta t) \right] \end{aligned} \quad (43c)$$

The Newton–Raphson iterative solver is used to solve the nonlinear equation (42) in two stages. In the first stage, equation (42) is solved for $\mathbf{S}(t + \Delta t)$, while the slip system resistance-related quantities, viz. $\rho^\alpha(t + \Delta t)$ for the unified flow rule, or $s^\alpha(t + \Delta t)$ for the phenomenological flow rule are held fixed. The equation for the i -th iteration is given as:

$$\mathbf{S}^{i+1}(t + \Delta t) = \mathbf{S}^i(t + \Delta t) - \mathbb{J}^{-1} : \mathbf{R}^i \quad (44)$$

where the residual \mathbf{R} and Jacobian \mathbb{J} are computed as:

$$\mathbf{R}^i = \mathbf{S}^i(t + \Delta t) - \mathbf{S}^{tr} + \sum_{\alpha=1}^{n_{slip}} \Delta \gamma^\alpha \mathbf{B}^\alpha \quad (45a)$$

$$\mathbb{J} = \frac{\partial \mathbf{R}}{\partial \mathbf{S}^i} = \mathbb{J}_{sym} + \sum_{\alpha=1}^{n_{slip}} \mathbf{B}^\alpha \otimes \frac{\partial \Delta \gamma^\alpha}{\partial \mathbf{S}^i} \quad (45b)$$

\mathbb{J}_{sym} is the fourth order symmetric identity tensor. Once $\mathbf{S}(t + \Delta t)$ is determined, the second stage calculates the evolution of the internal variables related to the slip system resistance. Subsequently, the first stage is repeated again with the evolved resistances. The sequence of computational operations needed for time integration of the constitutive relations is given in Table 2.

Table 2
Sequence of computational operations for the constitutive update procedure.

Step A Determine second Piola–Kirchhoff stress and slip rates.	
I	Initialize relevant quantities for the Newton–Raphson algorithm: $\mathbf{S}^0(t + \Delta t) = \mathbf{S}(t)$ $\rho^\alpha(t + \Delta t) = \rho^\alpha(t)$ (for unified flow rule) $s^\alpha(t + \Delta t) = s^\alpha(t)$ (for phenomenological flow rule)
II	For the i -th iteration in the Newton–Raphson algorithm: (a) Calculate the resolved shear stress using equation (9); (b) Evaluate the slip rate using equation (8) (for the unified flow rule) or equation (32) (for the phenomenological flow rule); (c) Update the second Piola–Kirchhoff stress using equation (44); (d) Check for convergence: if no, return to step (a); if yes, proceed to step III; Calculate the resolved shear stress and slip rate based on the converged second Piola–Kirchhoff stress.
Step B Update slip system resistances.	
IV	Compute hardening-related quantities: Evolve dislocation densities using equation (23) (for the unified flow rule) or calculate the hardening matrix using equation (34) (for the phenomenological flow rule).
V	Update slip system resistances: Use equation (29) (for the unified flow rule) or equation (33) (for the phenomenological flow rule);
VI	Check for convergence of slip system resistances: if no, return to step II; if yes, proceed to step VII.
VII	Evaluate elastic deformation gradient using equation (4) and Cauchy stress using equation (7).

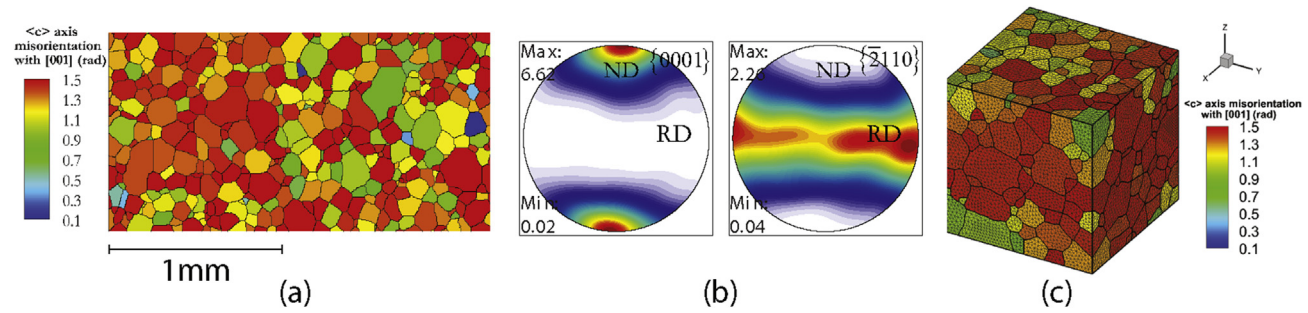


Fig. 5. (a) EBSD map of rolled-annealed Ti-7Al alloy microstructure, (b) pole figures extracted from the EBSD map, and (c) a statistically-equivalent polycrystalline microstructure containing 529 grains, discretized into TET4 elements.

Table 3

Elastic stiffness components at room temperature, experimentally measured in [Shade \(2015\)](#), and their reducing gradients with temperature reported in [Ogi et al. \(2004\)](#).

Parameter	Unit	$l\bar{l} = 11$	$l\bar{l} = 12$	$l\bar{l} = 13$	$l\bar{l} = 33$	$l\bar{l} = 55$
$C_{l\bar{l}}$	GPa	164.7	82.5	61.8	175.2	48.5
$\frac{\partial C_{l\bar{l}}}{\partial T}$	MPa/K	48	8.9	21	21	21.9

Table 4

Calibrated crystal plasticity parameters for the unified model for different slip systems.

Parameters	Unit	$\langle a \rangle$ – basal	$\langle a \rangle$ – prismatic	$\langle a \rangle$ – pyramidal	$\langle c + a \rangle$ – pyramidal
Q_{ref}^{α}	J	2.1×10^{-19}	2.2×10^{-19}	3.0×10^{-19}	2.6×10^{-19}
h_{kink}^{α}	b^{α}	20	20	20	20
S_{0s}^{α}	MPa	5.0	5.0	5.0	5.0
C_{ath}^{α}	–	0.8	0.62	0.7	0.5
C_{act}^{α}	–	0.7	0.7	0.1	0.04
C_l^{α}	–	8.0	8.0	8.0	8.0
C_{multi}^{α}	μm^{-1}	150	230	500	500
C_{annih}^{α}	–	10	10	10	10
C_Q^{α}	J	2.3×10^{-20}	3.7×10^{-20}	1.8×10^{-20}	0.9×10^{-20}
p_Q^{α}	–	1.6	1.6	1.6	1.6

Table 5

Calibrated crystal plasticity parameters for the phenomenological model for different slip systems.

Parameters	Unit	$\langle a \rangle$ – basal	$\langle a \rangle$ – prismatic	$\langle a \rangle$ – pyramidal	$\langle c + a \rangle$ – pyramidal
S_{0s}^{α}	MPa	230	205	500	610
$\dot{\gamma}_0^{\alpha}$	s^{-1}	0.003	0.003	0.003	0.003
h_{ref}^{α}	MPa	250	250	1200	2000
m	–	0.019	0.019	0.019	0.019
r^{α}	–	0.02	0.02	0.02	0.02
n^{α}	–	0.3	0.3	0.3	0.3
S^{α}	MPa	1600	1600	1600	1800

It should be pointed out that the inertia effects are ignored in the FEM level. While this does not hamper investigating how the mechanical response is affected by the choice of constitutive model at the integration-point level, it is imperative to take into account the inertial forces in the equilibrium equations for studying phenomena such as stress/shock waves in the medium.

5. Numerical results

Results of crystal plasticity FE simulations using the unified and phenomenological flow rules respectively are analyzed and compared for single crystal and polycrystalline microstructures, loaded at a range of strain-rates. The material studied is Ti-7.02Al-0.110-0.015Fe (wt%) or Ti-7Al alloy. It has a *hcp* crystalline microstructure, with a composition that is very close to the α phase of commercially available Ti alloys ([Pilchak, 2013](#)). [Fig. 5a](#) shows a 2 mm \times 1 mm 2D electron back-scattered diffraction (EBSD) surface map of a rolled-annealed (RA) Ti-7Al alloy, provided in [Pilchak \(2015\)](#), collected with step size of 5 μm in the orientation imaging microscopy system. The corresponding pole figures for the $\{0001\}$ and $\{2110\}$ orientations are shown in [Fig. 5b](#). Using this EBSD map, distributions of morphological and crystallographic parameters such as grain size, orientation and misorientation are developed using methods described in [Thomas et al. \(2012\)](#). The average grain size in 2D, defined as an equivalent circle diameter, is evaluated to be 83.4 μm . 3D statistical data are developed using stereological projection methods, and are subsequently used in the DREAM.3D software ([Groeber and Jackson, 2014; Groeber et al., 2008](#)) to re-construct a 3D statistically equivalent microstructures. Development of 3D statistics and microstructure reconstruction are discussed in part II of this paper ([Ghosh et al., 2016](#)). The statistically equivalent polycrystalline microstructure is discretized into linear tetrahedral elements (TET4) using the Simmetrix[®] software ([Simulation Modeling Suite, 2015](#)). [Fig. 5c](#) shows a statistically-equivalent microstructure of size 960 \times 960 \times 960 μm^3 containing 529 grains, discretized into 536090 TET4 elements.

Parameters in the unified and phenomenological flow rule based crystal plasticity relations are calibrated and validated using experiments conducted at a range of strain-rates. Details of the calibration and validation process are given in part II of this paper ([Ghosh et al., 2016](#)). Components of the elastic stiffness matrix C at room temperature in [Table 3](#), are taken from experimental measurements in ([Shade, 2015](#)) using resonant ultrasound spectroscopy. The effects of temperature on elastic constants can be significant under non-isothermal conditions, as experienced in high-rate simulations. The elastic constants have been found to decrease linearly with temperature in [Ogi et al. \(2004\)](#). The reducing slopes for the different elastic stiffness components with temperature is given in [Table 3](#). Various constitutive parameters for crystal plasticity models in section 2 with the unified and phenomenological flow rules, are respectively tabulated in [Tables 4 and 5](#).

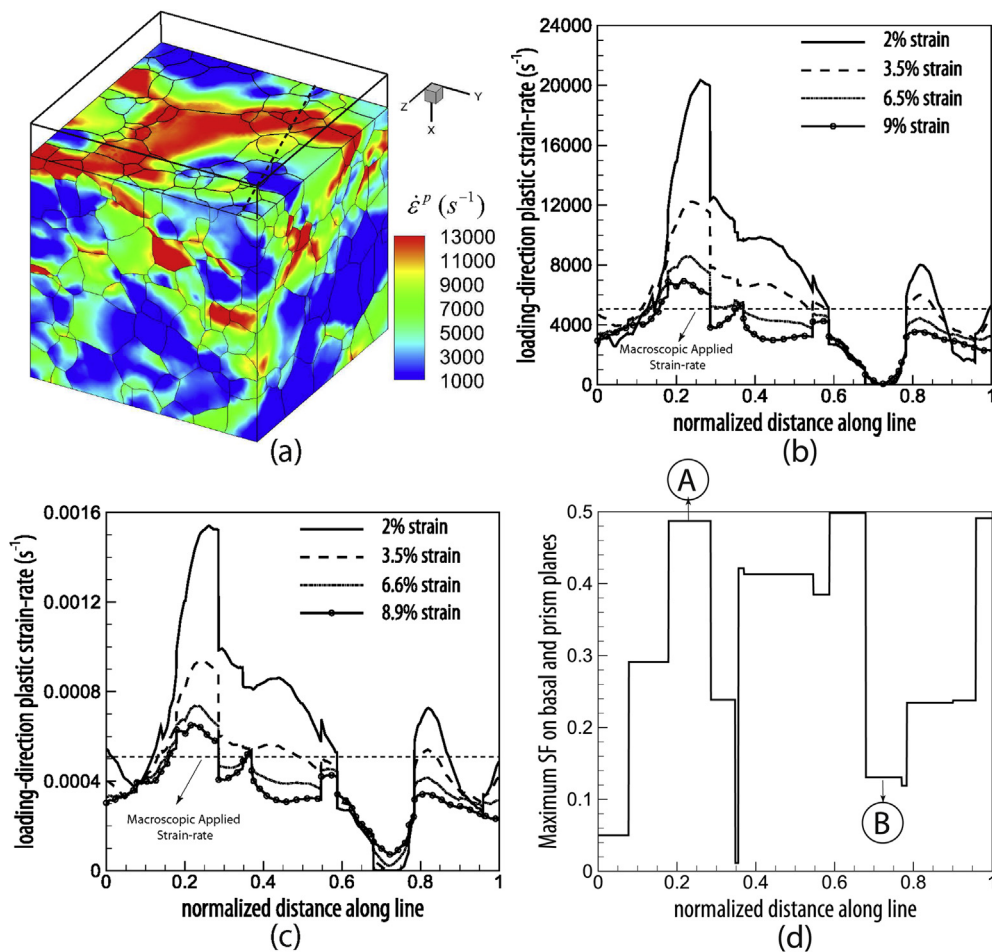


Fig. 6. (a) Contour plot of the loading-direction plastic strain-rate at 2% strain applied compressive strain-rate of $5 \times 10^3 s^{-1}$, plot of evolution of the loading-direction plastic strain-rate along the dashed line at different strain levels under an applied compressive strain-rate of (b) $5 \times 10^3 s^{-1}$, (c) $5 \times 10^{-4} s^{-1}$ and (d) maximum Schmid factor on the basal and prism planes along the dashed line.

5.1. Strain-rate variations in polycrystalline microstructures for CPFE simulations

The unified flow-rule is applicable to a wide range of applied strain-rates. Strain-rates at different locations in a heterogeneous and plastically anisotropic polycrystalline microstructure can vary significantly even for a uniformly applied macroscopic strain-rate. The unified flow-rule is uniquely capable of seamlessly accounting for the effects of location-dependent thermally-activated and drag-dominated mechanisms of dislocation glide without any user intervention. This capability is of importance in CPFE modeling, where the local strain-rates could be orders of magnitude different from the macroscopic applied strain-rate.

To investigate the distribution of the local strain-rate in a polycrystalline Ti-7Al microstructure, the CPFE simulation is conducted for an applied compressive strain-rate of $5 \times 10^3 s^{-1}$ along the X direction. Fig. 6a is a contour plot of the plastic strain-rate in the loading direction at 2% macroscopic strain. The heterogeneity in the strain-rate, especially over a plane parallel to the YZ plane is clearly depicted in this plot. Furthermore, the plastic strain-rate along the dashed line in Fig. 6a is plotted for different overall strain levels in Fig. 6b. The local plastic strain-rate field shows large variations at the early stages of plastic deformation. This variation decreases with increasing deformation. Fig. 6d shows the maximum Schmid factor on the basal and prism planes along the dashed line. Grains A and B in the plot have high and low values of the Schmid factor respectively, corresponding to most favorable and least favorable regions for time-dependent plastic deformation. The local plastic strain-rate in grain A reaches as high as ~5 times the macroscopic strain-rate at 2% strain. On the other hand, grain B is not favorably oriented for dislocation slip and the local plastic strain-rate in this grain ranges from 6 to 3 orders of magnitude lower than the macroscopic applied strain-rate, depending on the strain level. This observation is not only limited to high strain-rate deformations. Fig. 6c depicts the variation of local plastic strain-rate along the same line in the microstructure under an applied compressive strain-rate of $5 \times 10^{-4} s^{-1}$.

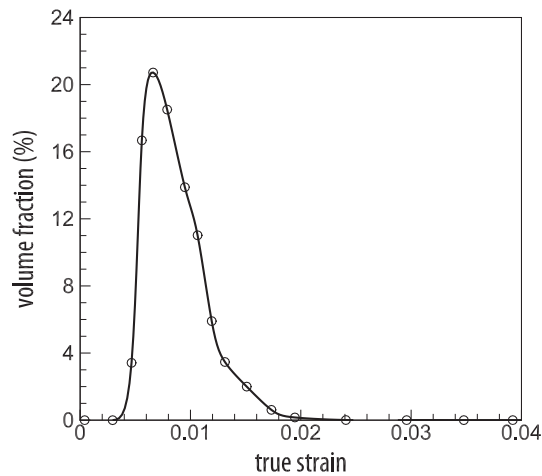


Fig. 7. Evolution of volume of fraction of elements with significant drag-dominated processes.

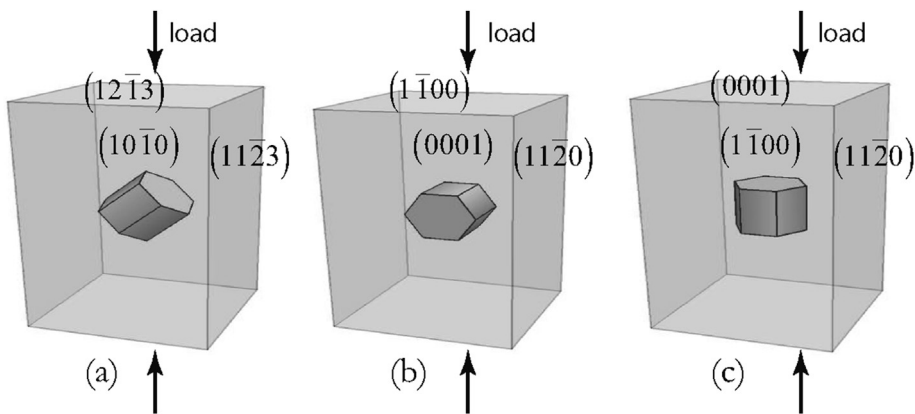


Fig. 8. Single crystal model oriented for dominant activation of (a) $\langle a \rangle$ – basal, (b) $\langle a \rangle$ – prismatic, and (c) $\langle c + a \rangle$ – pyramidal slip systems.

Table 6

Euler-angles and the maximum Schmid factor on different slip planes for different single crystal simulations.

	Fig. 8a	Fig. 8b	Fig. 8c
Euler-angles	$[0^\circ, 45^\circ, 30^\circ]$	$[0^\circ, 90^\circ, 0^\circ]$	$[0^\circ, 0^\circ, 0^\circ]$
max. SF on $\langle a \rangle$ – Basal	0.5	0.00	0.00
max. SF on $\langle a \rangle$ – Prism	0.22	0.43	0.00
max. SF on $\langle a \rangle$ – Pyramidal	0.31	0.38	0.00
max. SF on first-order $\langle c + a \rangle$ – Pyramidal	0.36	0.41	0.41
max. SF on second-order $\langle c + a \rangle$ – Pyramidal	0.28	0.34	0.45

Table 7

Schmid factors for the basal and prism slip families for the single crystal model oriented favorably for $\langle a \rangle$ – basal slip.

Slip system	Miller-Bravais index	Label	Schmid factor
Basal	$(0001)[\bar{1}210]$	B1	−0.25
	$(0001)[\bar{2}110]$	B2	0.50
	$(0001)[11\bar{2}0]$	B3	−0.25
Prism	$(10\bar{1}0)[\bar{1}2\bar{1}0]$	P1	0.22
	$(01\bar{1}0)[\bar{2}110]$	P2	0.00
	$(\bar{1}100)[\bar{1}120]$	P3	−0.22

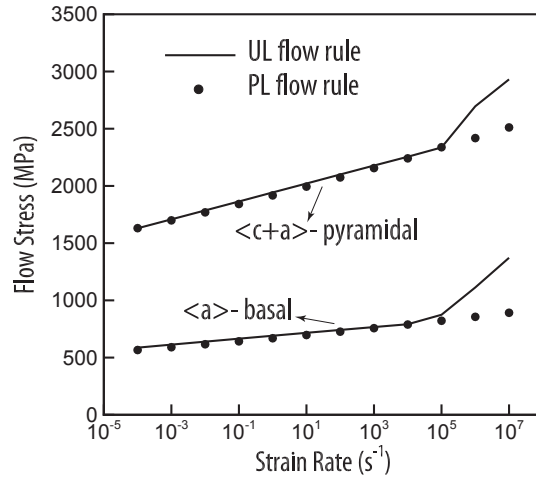


Fig. 9. Strain-rate sensitivity of flow stress in the single crystal model at 8% strain, as predicted by the unified (UL) and phenomenological (PL) models.

Next, the waiting (t_w^α) and running (t_r^α) times on individual slip systems are studied. To measure the relative effects of thermally-activated and drag-dominated processes, a *drag fraction* is introduced as the ratio of the time spent on the drag-dominated stage over the total travel time, i.e.

$$f_d^\alpha = \frac{t_r^\alpha}{(t_w^\alpha + t_r^\alpha)} \quad \text{s.t.} \quad 0 < f_d^\alpha \leq 1$$

The fraction is only defined for active slip systems. $f_d^\alpha \rightarrow 0$ corresponds to a predominantly thermally-activated dislocation glide, whereas $f_d^\alpha = 1$ denotes a purely drag-dominated dislocation glide. If f_d^α exceeds 0.1, the drag-dominated processes are significant as they constitute over 10% of the total dislocation travel time. Fig. 7 shows the evolution of volume fraction of elements with considerable drag-dominated dislocation glide. It is calculated by probing element integration points, for which $f_d^\alpha > 0.1$ on any active slip system. In the early stages of plastic deformation, the drag-dominated processes contribute to plasticity in up to 20% of the microstructural volume. With continuing deformation, the effects of drag-dominated processes gradually fade and the mode of dislocation glide smoothly transitions to a purely thermally-activated mode. The results demonstrate that the local state of the material points in the polycrystalline aggregates could be very different from the macroscopic applied loading and hence the need for the unified flow rule.

5.2. Rate sensitive flow rule in CPFE modeling of single crystals

To investigate the effectiveness of the rate-sensitive unified flow rule in CPFE modeling, uniaxial deformation simulation of single crystals are conducted. Three single crystal models with different orientations, illustrated in Fig. 8, are simulated in

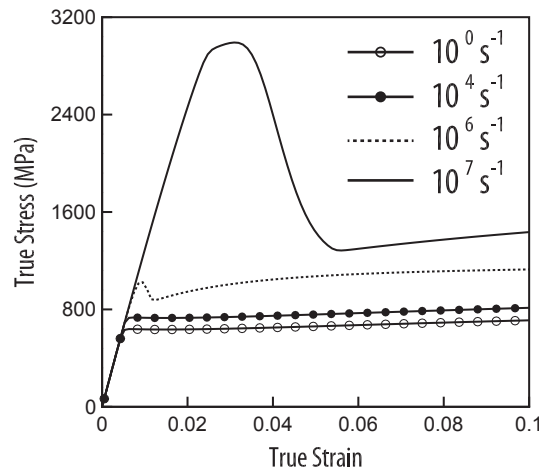


Fig. 10. Loading direction stress-strain response at different strain-rates for a single crystal model oriented favorably for (a)–basal slip.

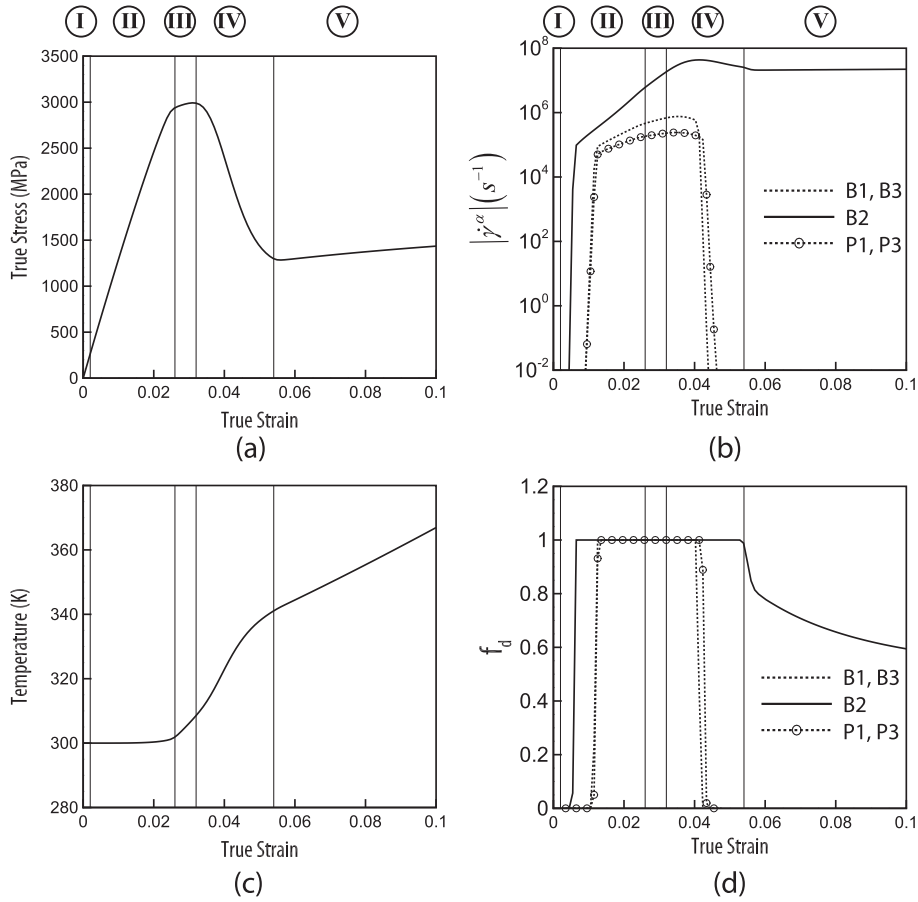


Fig. 11. Results of single crystal CPFE simulation for (a)– basal slip at strain rate of 10^7 s^{-1} : (a) the loading direction stress-strain response, and evolution of: (b) plastic shearing rate, (c) temperature and (d) drag fraction. (the Roman numerals denote different stages of deformation).

this study. The crystal models are oriented in a manner such that slip on specific crystallographic systems are dominant for each model. The corresponding Euler angles defining each orientation, along with the maximum Schmid factor (SF) on different slip planes are reported in Table 6.

The single crystal models are loaded under different strain-rates to comprehend the underlying dislocation glide behavior across a range of strain-rates. Fig. 9 shows the dependence of the flow stress on strain-rates ranging from 10^{-4} to 10^{+7} s^{-1} at 8% true strain, as predicted by the unified (UL) and phenomenological (PL) models. The resulting basal and pyramidal system

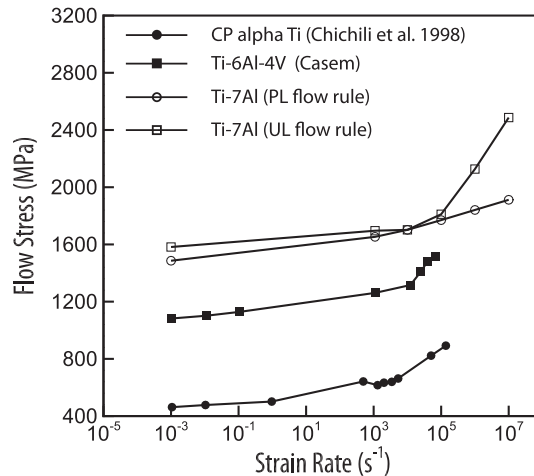


Fig. 12. Rate sensitivity of the flow stress in polycrystalline Ti alloys at 6% strain by the unified (UL) and phenomenological (PL) flow rules.

flow stresses exhibit a linear dependence on the logarithm of strain-rates. Predictions by the two models are in good agreement up to strain-rates of $\sim 10^5 \text{ s}^{-1}$. Beyond this, the slope predicted by the unified model is considerably higher than that by the phenomenological model. Similar trends are also observed for the prism dominated slip (not shown) and for other orientations. This change in the rate-sensitivity has also been observed for many metals e.g. in Follansbee et al. (1984). The results in Fig. 9 suggest that the phenomenological model can be reliably used up to strain-rates of $\sim 10^5 \text{ s}^{-1}$.

Fig. 10 depicts the loading direction stress-strain response for a single crystal model that is oriented favorably for $\langle a \rangle$ – basal slip, at a range of strain-rates. An elastic overshoot occurs in the stress response at strain-rates beyond 10^6 s^{-1} , which becomes more pronounced as the applied strain-rate is increased. Such elastic overshoot has been reported in simulations of copper (Hansen et al., 2013) and vanadium (Barton et al., 2011) at high deformation rates. The initial peak in the stress profile is explained in terms of dislocation activity on individual slip systems, which can be understood through a Schmid factor analysis given in Table 7. It indicates that the $[\bar{2}110]$ basal slip system has the highest Schmid factor, leading to a dominant single-slip mode. Slip activities on the $\langle a \rangle$ – pyramidal and $\langle c + a \rangle$ – pyramidal systems are relatively dormant for this loading case.

5.2.1. Evolution of temperature and plastic strains in single crystals

Fig. 11 shows the evolution of temperature, plastic shearing-rate and drag fraction on the basal and prism slip system families at a strain-rate of 10^7 s^{-1} . All slip systems in the basal and prism families become active with deformation except for P2. Consequently, it is not included in the plots in Fig. 11. The overall deformation may be generally partitioned into multiple stages, as enumerated in Fig. 11. Stage I corresponds to a purely elastic regime where the resolved shear stress on all slip systems is smaller than the long-range stress, viz. the passing stress τ_{pass}^α that occurs by interaction of mobile dislocations with other dislocations and their networks. In stage II, dislocation slip starts to occur on B2. However, the initial dislocation density is not sufficient to sustain plastic deformation for the applied strain-rate. The material should deform elastically until a sufficient amount of dislocation density is available. This translates into an increase in the stress level and consequently provides adequate resolved shear stress to activate the other basal and prism slip systems with lower Schmid factors, as shown in Fig. 11b. Fig. 11d shows the transition of dislocation glide from a thermally-activated to drag-dominated mechanism in this stage. In stage III, there is collectively sufficient dislocation content to cause plastic shearing for the applied strain-rate. Thus the macroscopic stress-strain response deviates clearly from a predominantly elastic response. During this stage, drag-dominated dislocation glide persists and plastic shearing rate on active slip systems, specifically on B2, increases. This causes the self and latent hardening to become more pronounced. Fig. 11c shows the evolution of temperature in this stage due to the significant development of plastic and dissipative work. During stage IV, dislocation glide on B2 remains drag-dominated and sufficient dislocation density accumulates on B2 to accommodate further plastic deformation. This causes a drop in the stress level in this stage. As the stress decreases, the plastic contribution of slip systems with lower Schmid factor, viz. B1, B3, P1 and P3, progressively reduces until these slip systems become inactive at the end of this stage. In Stage V, B2 is the sole active slip system. Self hardening through the evolution of the parallel dislocation population is the main source of strain hardening, as observed in Fig. 11a. During this step, thermally-activated processes become more significant, and the mechanism governing dislocation glide transitions from a drag-dominated mode to a mixed mode.

The high stresses induced by the elastic overshoot at very high strain-rates can be relieved in real materials by either nucleating new dislocations (in addition to dislocation multiplication) (Austin and McDowell, 2011) or by deformation twinning (Follansbee and Gray, 1989; Chichili et al., 1998; Morrow et al., 2016). Considering the contributions of homogeneous and heterogeneous dislocation nucleation to the evolution of dislocation population may be of benefit in the simulation of polycrystals subject to very high strain-rates and shock loading (Meyers et al., 2003; Capolungo et al., 2007). The model in this paper considers dislocation slip as the major deformation mechanism, based on experimental results in Paton et al. (1976) and Williams et al. (2002) where twinning was not reported for Ti alloys with high Al concentration.

5.3. Rate sensitive flow rule in CPFE modeling of polycrystals

Experiments on polycrystalline Ti samples have shown an increasing rate sensitivity to the logarithm of strain-rate (Chichili et al., 1998). Based on the rate sensitivity study of single crystals, it is expected that the unified model will show the change in rate sensitivity of flow stress for polycrystalline microstructures. The polycrystalline Ti-7Al microstructural volume, shown in Fig. 5c, is compressed in the X direction (the ND direction) at various strain-rates. The flow stress from the CPFE analyses at 6% strain is plotted in Fig. 12. These results are compared with some experimental results for Ti-6Al-4V in Casem (2015) and commercially-pure Ti (Chichili et al., 1998). Results with the unified model show a change in the rate sensitivity for strain-rates higher than 10^5 s^{-1} . This is in good agreement with the experimental results of Casem (2015), where an enhanced hardening effect is observed beyond strain rates of 10^4 s^{-1} . The phenomenological model exhibits a constant rate sensitivity across a range of strain-rates.

6. Concluding remarks

The first of this two part paper develops a framework for a unified crystal plasticity constitutive model that can transcend a wide range of strain-rates, for which different mechanisms are known to govern plastic flow. The unified flow rule is given in the form of the Orowan equation, which expresses the slip rate in terms of the dislocation density and average dislocation

velocity. Dislocation motion on glide planes is controlled by thermal activation and drag mechanisms, with relative strengths that depend on the level of stress and strain-rate. The screw dislocation motion in the glide plane is assumed to take place in two successive stages. The first involves waiting in a Peierls valley until thermal activation nucleates a kink pair for moving to the next valley. In the subsequent drag-dominated stage, the kinks move apart and bring the dislocation line to the next Peierls valley. Unified flow rule accounts for this by combining an Arrhenius type thermal activation-based flow rule with a viscous drag dominated linear flow rule. The resulting model is capable of simulating across orders of magnitude in the strain-rate with smooth transition from the thermally-activated to drag-dominated stage and vice-versa. Generally this transition is found to occur in the neighborhood of 10^4 – 10^5 s⁻¹ for the Ti alloys considered in this study. Temperature dependence in the form of thermal activation makes the model effective for simulating temperature-sensitive phenomena. The model also explicitly accounts for temperature change due to dissipation of plastic work leading to adiabatic heating. This in turn, promotes additional plastic deformation through increase in the rate of thermal activation. The unified constitutive model is implemented in a crystal plasticity finite element framework for simulating deformation in polycrystalline materials.

CPFE simulations are conducted for single crystal and polycrystalline Ti alloy, Ti-7Al. The simulations demonstrate the large variation in strain-rates across the microstructure due to local plastic anisotropy and heterogeneity. A simple phenomenological flow rule may not have the capability to handle this variability. The unified model can effectively capture the increase in the rate sensitivity of the flow stress at higher rates of deformation due to the transition in the rate controlling mechanism of dislocation motion. For single crystals, the model predicts an elastic overshoot under very high strain-rates due to the insufficient dislocation content that can accommodate the applied strain rate. For the polycrystalline model, simulations with the unified model show a change in the rate sensitivity of flow stress across decades of strain-rates, which is consistent with experiments. The part II of this paper (Ghosh et al., 2016) is dedicated to the development of an image-based CPFE model of polycrystalline Ti-7Al for calibration and validation with experiments at different strain-rates.

Acknowledgments

This work has been supported by the Army Research Office through grant No. W911NF-12-1-0376 (Program Manager: Dr. A. Rubinstein) and by the Office of Naval research through grant No. N00014-15-1-2040 (Program Manager: Mr. W. Nickerson). Computing support by the Homewood High Performance Compute Cluster (HHPC) and the Maryland Advanced Research Computing Center (MARCC) is gratefully acknowledged.

References

- Akhtar, A., Teghtsoonian, E., 1975. Prismatic slip in α -titanium single crystals. *Metall. Mater. Trans. A* 6, 2201–2208.
- Alankar, A., Eisenlohr, P., Raabe, D., 2011. A dislocation density-based crystal plasticity constitutive model for prismatic slip in α -titanium. *Acta Mater.* 59 (18), 7003–7009.
- Anahid, M., Samal, M., Ghosh, S., 2011. Dwell fatigue crack nucleation model based on crystal plasticity finite element simulations of polycrystalline titanium alloys. *J. Mech. Phys. Solids* 59 (10), 2157–2176.
- Arsenlis, A., Parks, D.M., 1998. Crystallographic aspects of geometrically-necessary and statistically-stored dislocation density. *Acta Mater.* 47, 1597–1611.
- Asaro, R., Rice, J., 1977. Strain localization in ductile single crystals. *J. Mech. Phys. Solids* 25 (5), 309–338.
- Austin, R., McDowell, D., 2011. A dislocation-based constitutive model for viscoplastic deformation of fcc metals at very high strain rates. *Int. J. Plast.* 27 (1), 1–24.
- Balasubramanian, S., Anand, L., 2002. Plasticity of initially textured hexagonal polycrystals at high homologous temperatures: application to titanium. *Acta Mater.* 50 (1), 133–148.
- Barton, N., Bernier, J., Becker, R., Arsenlis, A., Cavallo, R., Marian, J., Rhee, M., Park, H., Remington, B., Olson, R., 2011. A multiscale strength model for extreme loading conditions. *J. Appl. Phys.* 109 (7), 073501.
- Becker, R., Arsenlis, A., Marian, J., Rhee, M., Tang, M., Yang, L., 2009. Continuum Level Formulation and Implementation of a Multi-scale Model for Vanadium. Technical report. Lawrence Livermore National Laboratory.
- Brandes, M., 2008. Creep, Fatigue, and Deformation of Alpha and Alpha-beta Titanium Alloys at Ambient Temperature. Ph.D. thesis. Materials science and engineering, Ohio State University, USA.
- Capolungo, L., Spearot, D., Cherkaoui, M., McDowell, D., Qu, J., Jacob, K., 2007. Dislocation nucleation from bicrystal interfaces and grain boundary ledges: relationship to nanocrystalline deformation. *J. Mech. Phys. Solids* 55 (11), 2300–2327.
- Casem, D. (2015). Unpublished work.
- Cheng, J., Ghosh, S., 2015. A crystal plasticity FE model for deformation with twin nucleation in magnesium alloys. *Int. J. Plast.* 67, 148–170.
- Cheng, J., Shahba, A., Ghosh, S., 2016. Stabilized tetrahedral elements for crystal plasticity finite element analysis overcoming volumetric locking. *Comput. Mech.* 57 (5), 733–753.
- Chichili, D., Ramesh, K., Hemker, K., 1998. The high-strain-rate response of alpha-titanium: experiments, deformation mechanisms and modeling. *Acta Mater.* 46 (3), 1025–1043.
- Clayton, J., 2005. Dynamic plasticity and fracture in high density polycrystals: constitutive modeling and numerical simulation. *J. Mech. Phys. Solids* 53, 261301.
- Clayton, J., 2010. *Nonlinear Mechanics of Crystals*. Springer Verlag.
- Dai, H., 1997. Geometrically-necessary Dislocation Density in Continuum Plasticity Theory, FEM Implementation and Applications. Ph.D. thesis. Department of Mechanical Engineering, Massachusetts Institute of Technology, USA.
- de Souza Neto, E.A., Pires, F.M.A., Owen, D.R.J., 2005. F-bar-based linear triangles and tetrahedra for finite strain analysis of nearly incompressible solids. Part I: formulation and benchmarking. *Int. J. Numer. Meth. Eng.* 62 (3), 353–383.
- Deka, D., Joseph, D.S., Ghosh, S., Mills, M.J., 2006. Crystal plasticity modeling of deformation and creep in polycrystalline Ti-6242. *Metall. Trans. A* 37A (5), 1371–1388.
- Dunne, F., Rugg, D., Walker, A., 2007. Length scale-dependent, elastically anisotropic, physically-based hcp crystal plasticity: application to cold-dwell fatigue in Ti alloys. *Int. J. Plast.* 23 (6), 1061–1083.
- Essmann, U., Mughrabi, H., 1979. Annihilation of dislocations during tensile and cyclic deformation and limits of dislocation densities. *Phil. Mag. A* 40 (6), 731–756.
- Follansbee, P., Gray, G., 1989. An analysis of the low temperature, low and high strain-rate deformation of Ti-6Al-4V. *Metall. Trans. A* 20, 863–874.

- Follansbee, P., Regazzoni, G., Kocks, U., 1984. Mechanical properties at high rates of strain. In: Proceedings of the Third Conference on the Mechanical Properties of Materials at High Rates of Strain Held in Oxford, 9–12 April 1984. Conference Series, Inst. of Physics.
- Frost, H.J., Ashby, M.F., 1971. Motion of a dislocation acted on by a viscous drag through an array of discrete obstacles. *J. Appl. Phys.* 42 (13), 5273–5279.
- Ghosh, S., Shahba, A., Tu, X., Huskins, E., Schuster, B., 2016. Crystal plasticity FE modeling of Ti Alloys for a range of strain-rates. Part II: image-based model with experimental validation. *Int. J. Plast.* 87, 69–85. <http://dx.doi.org/10.1016/j.iijplas.2016.09.003>.
- Groeber, M., Ghosh, S., Uchic, M., Dimiduk, D., 2008. A framework for automated analysis and representation of 3d polycrystalline microstructures, Part 1: statistical characterization. *Acta Mater.* 56, 1257–1273.
- Groeber, M., Jackson, M., 2014. DREAM.3D: a digital representation environment for the analysis of microstructure in 3D. *Integr. Mater. Manuf. Innov.* 3 (5), 1–17.
- Guyot, P., Dorn, J., 1967. A critical review of the Peierls mechanism. *Can. J. Phys.* 45 (2), 983–1016.
- Hansen, B., Beyerlein, I., Bronkhorst, C., Cerreta, E., Dennis-Koller, D., 2013. A dislocation-based multi-rate single crystal plasticity model. *Int. J. Plast.* 44, 129–146.
- Hasija, V., Ghosh, S., Mills, M.J., Joseph, D.S., 2003. Deformation and creep modeling in polycrystalline Ti6Al alloys. *Acta Mater.* 51, 4533–4549.
- Hiratani, M., Nadgorny, E., 2001. Combined model of dislocation motion with thermally activated and drag-dependent stages. *Acta Mater.* 49 (20), 4337–4346.
- Hiratani, M., Zbib, H., Khaleel, M., 2003. Modeling of thermally activated dislocation glide and plastic flow through local obstacles. *Int. J. Plast.* 19 (9), 1271–1296.
- Isaac, R.D., Granato, A.V., 1988. Rate theory of dislocation motion: Thermal activation and inertial effects. *Phys. Rev. B* 37, 9278–9285.
- Keshavarz, S., Ghosh, S., 2013. Multi-scale crystal plasticity finite element model approach to modeling nickel-based superalloys. *Acta Mater.* 61 (17), 6549–6561.
- Khan, A., Kazmi, R., Farrokh, B., 2007. Multiaxial and non-proportional loading responses, anisotropy and modeling of Ti6Al4V titanium alloy over wide ranges of strain rates and temperatures. *Int. J. Plast.* 23 (6), 931–950.
- Khan, A., Suh, Y., Kazmi, R., 2004. Quasi-static and dynamic loading responses and constitutive modeling of titanium alloys. *Int. J. Plast.* 20 (12), 2233–2248.
- Khan, A., Yu, S., 2012. Deformation induced anisotropic responses of Ti6Al4V alloy. Part I Exp. *Int. J. Plast.* 38, 1–13.
- Kocks, U., Argon, A., Ashby, M., 1975. Thermodynamics and kinetics of slip. *Prog. Mater. Sci.* 19.
- Lee, B., Vecchio, K., Ahzi, S., Schoenfeld, S., 1997. Modeling the mechanical behavior of tantalum. *Metal. Mater. Trans. A* 28 (1), 113–122. ISSN 1073-5623.
- Li, H., Mason, D., Bieler, T., Boehler, C., Crimp, M., 2013. Methodology for estimating the critical resolved shear stress ratios of α -phase Ti using EBSD-based trace analysis. *Acta Mater.* 61 (20), 7555–7567.
- Ling, X., Horstemeyer, M.F., Potirniche, G.P., 2005. On the numerical implementation of 3D rate-dependent single crystal plasticity formulations. *Int. J. Numer. Meth. Eng.* 63 (4), 548–568.
- Lloyd, J., Clayton, J., Austin, R., McDowell, D., 2014. Plane wave simulation of elastic-viscoplastic single crystals. *J. Mech. Phys. Solids* 69, 14–32.
- Ma, A., Roters, F., Raabe, D., 2006. A dislocation density based constitutive model for crystal plasticity FEM including geometrically necessary dislocations. *Acta Mater.* 54 (8), 2169–2179.
- Matous, K., Maniatty, A., 2004. Finite element formulation for modelling large deformations in elasto-viscoplastic polycrystals. *Int. J. Numer. Meth. Eng.* 60, 2313–2333.
- Mecking, H., Kocks, U., 1981. Kinetics of flow and strain-hardening. *Acta Metal.* 29 (11), 1865–1875.
- Meissonnier, F., Busso, E., O'Dowd, N., 2001. Finite element implementation of a generalised non-local rate-dependent crystallographic formulation for finite strains. *Int. J. Plast.* 17, 601–640.
- Meyers, M., Gregori, F., Kad, B., Schneider, M., Kalantar, D., Remington, B., Ravichandran, G., Boehly, T., Wark, J., 2003. Laser-induced shock compression of monocrystalline copper: characterization and analysis. *Acta Mater.* 51 (5), 1211–1228.
- Military Handbook, 1998. Metallic Materials and Elements for Aerospace Vehicle Structures. Wright Lab., Wright-Patterson AFB, OH. Materials Directorate.
- Montgomery, J., Wells, M., Roopchand, B., Ogilvy, J., 1997. Low-cost titanium armors for combat vehicles. *JOM* 49 (5), 45–47.
- Morrow, B., Lebensohn, R., Trujillo, C., Martinez, D., Addessio, F., Bronkhorst, C., Lookman, T., Cerreta, E., 2016. Characterization and modeling of mechanical behavior of single crystal titanium deformed by split-Hopkinson pressure bar. *Int. J. Plast.* 82, 225–240.
- Neeraj, T., Mills, M., 2001. Short-range order (SRO) and its effect on the primary creep behavior of a Ti6wt. % Al alloy. *Mater. Sci. Eng. A* 319321, 415–419.
- Nemat-Nasser, S., Guo, W., Cheng, J., 1999. Mechanical properties and deformation mechanisms of a commercially pure titanium. *Acta Mater.* 47 (13), 3705–3720.
- Nie, Y., Xie, Y., 2007. *Ab initio* thermodynamics of the hcp metals Mg, Ti, and Zr. *Phys. Rev. B* 75, 174117.
- Nizhankovskii, V., Katsnelson, M., Peschanskikh, G., Trefilov, A., 1994. Anisotropy of the thermal-expansion of titanium due to proximity to an electronic topological transition. *JETP Lett.* 59, 733–737.
- Ogi, H., Kai, S., Ledbetter, H., Tarumi, R., Hirao, M., Takashima, K., 2004. Titaniums high-temperature elastic constants through the hcpbcc phase transformation. *Acta Mater.* 52 (7), 2075–2080.
- Paton, N., Baggerly, R., Williams, J., 1976. Deformation and Solid Solution Strengthening of Titanium-aluminum Single Crystals. Technical report, Rockwell Int. Report.
- Peirce, D., Asaro, R., Needleman, A., 1982. An analysis of nonuniform and localized deformation in ductile single crystals. *Acta Metal.* 30 (6), 1087–1119.
- Pilchak, A., 2013. Fatigue crack growth rates in alpha titanium: faceted vs. striation growth. *Scr. Mater.* 68 (5), 277–280.
- Pilchak, A. (2015). Unpublished Report.
- Ravichandran, G., Rosakis, A.J., Hodowany, J., Rosakis, P., 2002. On the conversion of plastic work into heat during high-strain-rate deformation. In: Shock Compression of Condensed Matter, Volume 620 of American Institute of Physics Conference Series, pp. 557–562.
- Schoenfeld, S., Kad, B., 2002. Texture effects on shear response in Ti6Al4V plates. *Int. J. Plast.* 18, 461–486.
- Shade, P. (2015). Unpublished work.
- Simulation Modeling Suite, 2015. Simmetrix Inc. <http://www.simmetrix.com>.
- Sinha, V., Mills, M., Williams, J., 2007. Determination of crystallographic orientation of dwell-fatigue fracture facets in Ti-6242 alloy. *J. Mater. Sci.* 42 (19), 8334–8341.
- Souvatzi, P., Eriksson, O., Katsnelson, M.I., 2007. Anomalous Thermal expansion in α -Titanium. *Phys. Rev. Lett.* 99, 015901.
- Tanaka, T., Conrad, H., 1972. Deformation kinetics for $10\bar{1}01120$ slip in titanium single crystals below $0.4 T_m$. *Acta Metal.* 20 (8), 1019–1029.
- Tang, M., Kubin, L., Canova, G., 1998. Dislocation mobility and the mechanical response of b.c.c. single crystals: a mesoscopic approach. *Acta Mater.* 46 (9), 3221–3235.
- Thomas, J., Groeber, M., Ghosh, S., 2012. Image-based crystal plasticity FE framework for microstructure dependent properties of Ti6Al4V alloys. *Mater. Sci. Eng. A* 553 (15), 164–175.
- Venkataramani, G., Ghosh, S., Mills, M.J., 2007. A size dependent crystal plasticity finite element model for creep and load-shedding in polycrystalline Titanium alloys. *Acta Mater.* 55, 3971–3986.
- Venkataramani, G., Kirane, K., Ghosh, S., 2008. Microstructural parameters affecting creep induced load shedding in Ti-6242 by a size dependent crystal plasticity FE model. *Int. J. Plast.* 24, 428–454.
- Williams, J., Baggerly, R., Paton, N., 2002. Deformation behavior of HCP Ti-Al alloy single crystals. *Metall. Mater. Trans. A* 33, 837–850.
- Zienkiewicz, O., Zhu, J., 1992. The superconvergent patch recovery (SPR) and adaptive finite element refinement. *Comput. Meth. Appl. Mech. Eng.* 101 (13), 207–224.